White Rose Research Online

eprints@whiterose.ac.uk
https://eprints.whiterose.ac.uk
Universities of Leeds, Sheffield and York

Deposited via The University of Sheffield.

White Rose Research Online URL for this paper:
https://eprints.whiterose.ac.uk/id/eprint/224896/

Version: Published Version

Article:
Lyman, J.D., Dhillon, V.S., Kamann, S. et al. (2025) Constraints on optical and near-infrared variability in the localization of the long-period radio transient GLEAM-X J1627−52. Monthly Notices of the Royal Astronomical Society, 538 (2). pp. 925-942. ISSN: 0035-8711

https://doi.org/10.1093/mnras/staf325

Reuse
This article is distributed under the terms of the Creative Commons Attribution (CC BY) licence. This licence allows you to distribute, remix, tweak, and build upon the work, even commercially, as long as you credit the authors for the original work. More information and the full terms of the licence here: https://creativecommons.org/licenses/

Takedown
If you consider content in White Rose Research Online to be in breach of UK law, please notify us by emailing eprints@whiterose.ac.uk including the URL of the record and the reason for the withdrawal request.

UNIVERSITY OF LEEDS
University of Sheffield
UNIVERSITY of York

Monthly Notices of the ROYAL ASTRONOMICAL SOCIETY

MNRAS **538,** 925–942 (2025) https://doi.org/10.1093/mnras/staf325
Advance Access publication 2025 February 21

Constraints on optical and near-infrared variability in the localization of the long-period radio transient GLEAM-X J1627−52

J. D. Lyman [1]★ V. S. Dhillon [2,3] S. Kamann [4] A. A. Chrimes,[5,6] A. J. Levan,[1,6] I. Pelisoli [1] D. T. H. Steeghs [1] and K. Wiersema[7]

[1]*Department of Physics, University of Warwick, Coventry CV4 7AL, UK*
[2]*Astrophysics Research Cluster, School of Mathematical and Physical Sciences, University of Sheffield, Sheffield S3 7RH, UK*
[3]*Instituto de Astrofísica de Canarias, E-38205 La Laguna, Tenerife, Spain*
[4]*Astrophysics Research Institute, Liverpool John Moores University, IC2 Liverpool Science Park, 146 Brownlow Hill, Liverpool L3 5RF, UK*
[5]*European Space Agency (ESA), European Space Research and Technology Centre (ESTEC), Keplerlaan 1, NL-2201 AZ Noordwijk, The Netherlands*
[6]*Department of Astrophysics/IMAPP, Radboud University Nijmegen, PO Box 9010, NL-6500 GL Nijmegen, The Netherlands*
[7]*Centre for Astrophysics Research, University of Hertfordshire, Hatfield AL10 9AB, UK*

Accepted 2025 February 19. Received 2025 February 17; in original form 2024 December 10

ABSTRACT

GLEAM-X J1627−52 was discovered as a periodic (∼18 min) radio signal over a duration of three months in 2018. It is an enigmatic example of a growing population of 'long-period radio transients' consistent with Galactic origins. Their nature is uncertain, and leading models invoke magnetic neutron stars or white dwarfs, potentially in close binary systems, to power them. GLEAM-X J1627−52 resides in the Galactic plane with a comparatively coarse localization (≃2 arcsec). Here, we study the localization region to search for spectrophotometric signatures of a counterpart using time-domain searches in optical and near-infrared imaging, and MUSE integral field spectroscopy. No sources in the localization display clear white dwarf spectral signatures, although at the expected distance we can only provide modest limits on their presence directly. We rule out the presence of hot subdwarfs in the vicinity. We found no candidate within our search for variability or periodic behaviour in the light curves. Radial velocity curves additionally show only weak evidence of variation, requiring any realistic underlying system to have very low orbital inclination ($i \lesssim 5$ deg). Two Balmer emission line sources are reminiscent of white dwarf pulsar systems, but their characteristics fall within expected M-dwarf chromospheric activity with no signs of being in a close binary. Currently the white dwarf pulsar scenario is not supported, although longer baseline data and data contemporaneous with a radio active epoch are required before stronger statements. Isolated magnetars, or compact binaries remain viable. Our limits highlight the difficulty of these searches in dense environments at the limits of ground-based data.

Key words: binaries: close – stars: magnetars – stars: neutron – white dwarfs – radio continuum: transients.

1 INTRODUCTION

Cadenced wide-field radio surveys at both high and low frequencies are beginning to probe the variable and transient radio sky over increasingly wide ranges of time-scales and luminosities. Well-established Galactic populations of pulsars (Manchester et al. 2005) and magnetars (Olausen & Kaspi 2014) have been known for many years and are seen to display periodicity of emission on time-scales of $\lesssim$10 s. Conversely, a small subset of the more-recently discovered extragalactic fast radio bursts (FRBs) show repeating bursts on time-scales of $\sim 0.4 - 40$ d (Chime/Frb Collaboration 2023, although notable exceptions have displayed bursts at higher rates for periods of time, e.g. Lanman et al. 2022). Rotating (and magnetized) neutron stars (NSs) naturally explain these Galactic populations (e.g. Lyne, Manchester & Taylor 1985; Thompson & Duncan 1995) and are also a leading model for repeating FRBs (Cordes & Chatterjee 2019). Between these two time-scales, an emerging population of long-period Galactic radio transients is been revealed (e.g. Hyman et al. 2005; Caleb et al. 2022; Hurley-Walker et al. 2023, 2024; Dong et al. 2024; Li et al. 2024; de Ruiter et al. 2024; Lee et al. 2025) that is challenging current models. The population is grouped on displaying periodic coherent radio emission on minutes to hour time-scales, however they are otherwise relatively heterogeneous. Some sources display regular period emission over long time-scales (years), with others seemingly active only for short periods and/or showing only intermittent burst emission. The pulse profiles of the emission are also characteristically diverse, even for a given source. Rotating Radio Transients (McLaughlin et al. 2006) share some of these characteristics, albeit without clear periodicity in the burst emission, a defining characteristic of these long-period radio transients.

Among the emerging population of long-period Galactic radio transients is GLEAM-X J162759.5−523504.3 (hereafter GLEAM-X J1627−52). Reported by Hurley-Walker et al. (2022), GLEAM-X J1627−52 is a Galactic Plane source at a distance of

★ E-mail: J.D.Lyman@warwick.ac.uk

© 2025 The Author(s).
Published by Oxford University Press on behalf of Royal Astronomical Society. This is an Open Access article distributed under the terms of the Creative Commons Attribution License (https://creativecommons.org/licenses/by/4.0/), which permits unrestricted reuse, distribution, and reproduction in any medium, provided the original work is properly cited.

Downloaded from https://academic.oup.com/mnras/article/538/2/925/8029896 by guest on 26 March 2025

1.3 ± 0.4 kpc, displaying heterogeneous pulse profiles with a period $P = 1091.169$ s, which was seemingly active for only three months in early 2018. A strong linear polarization of the pulses was used to infer the presence of strong magnetic fields, with rapid variability indicating a compact emitting region. Taken together, Hurley-Walker et al. (2022) use these arguments to favour a magnetar origin for the emission.

The rotation rate of magnetars slows over time due to energy losses, mainly magnetic dipole emission (Pacini 1967) and a measure of the current spin period and its derivative under this model can be used to infer the age and magnetic field strength of the magnetar (Duncan & Thompson 1992). Additionally, as the period of pulsar and magnetar emission is determined by their spin, ∼minutes–hour long periodicity of emission would typically be way beyond the pulsar 'death line' (Chen & Ruderman 1993) where emission is expected to cease, except for extreme magnetic field strengths. Following this, the properties of GLEAM-X J1627−52 suggest it may have $B \gtrsim 10^{16}$ G, and consequently, the most magnetized NS known (Konar 2023; Suvorov & Melatos 2023). GLEAM-X J1627−52 is therefore of chief interest for understanding the evolution of compact objects as the final stages of stellar evolution, with implications for other transient populations (Beniamini et al. 2023). It is possible to produce such long-period systems in the magnetar scenario via fallback disc braking (Chatterjee, Hernquist & Narayan 2000). Indeed, the fallback accretion scenario as a braking mechanism is the favoured model to explain the slowest rotational period magnetar, with a period of 6.7 h (Rea et al. 2016). As noted by Tong (2023), GLEAM-X J1627−52 may then represent an intermediate object in a poorly observed regime between the extrema of magnetar periods observed. Using population synthesis, Rea et al. (2024) recently conclude that isolated NSs, emitting as the classical rotating dipole pulsar, are an unlikely scenario to explain most, if not all, long-period radio transients.

Other analyses have favoured a highly magnetized white dwarf (WD) or hot subdwarf origin for GLEAM-X J1627−52 (e.g. Katz 2022; Loeb & Maoz 2022) wherein the large moment of inertia of the stellar system (cf. that of an NS) provides a sufficient rotational energy reservoir to power the observed radio emission. However, as noted by Konar (2023), the required magnetic field strengths remain significantly larger than those seen in typical WD or hot subdwarf systems. Periodic radio emission has been seen in three WD systems. The AR Sco (Marsh et al. 2016) and J1912 − 4410 (Pelisoli et al. 2023) systems display dominant periodic emission on minutes time-scale (associated with the WD spin), with hours-long modulation on the time–scale of their orbits with low-mass non-degenerate companions, and form a class of 'WD pulsar'. Conversely, the recently discovered ILT J1101 + 5521 system (Ruiter et al. 2024) displays periodic emission on a 125.5 min time-scale that matches the orbital period of the system. In the former systems, the leading explanations for the pulsed radio emission require interaction between the WD and its non-degenerate companion – either through magnetic reconnection between the fields of the WD and the companion producing synchrotron emission (e.g Katz 2017; Garnavich et al. 2019), or through electron–cyclotron maser when particles seeded by the companion reach the WD polar region (Pelisoli et al. 2024). In ILT J1101 + 5521, the origin is even less clear, although the binary is likely to be in a polar configuration with a moderately magnetic WD, which could produce radio pulses due to geometry effects of a beam sweeping with the orbit.

As with many astrophysical phenomena, unlocking the true nature of long-period radio transients may be largely contingent on multiwavelength characterization. This will allow for the nature of their underlying systems and powering mechanisms to be uncovered, and ultimately place them in the landscape of stellar and compact object evolution. Unfortunately, observationally and/or intrinsically rare Galactic phenomena are typically found in areas of high stellar density and line-of-sight extinction, hampering optical and near-infrared (NIR) counterpart searches.

GPM J1839−10 (Hurley-Walker et al. 2023), which displays ∼minute long radio bursts on a 21 min period and has been active for at least 30 yr, has a promising candidate K/M-dwarf NIR counterpart identified. The large distance to this object (5.7 ± 2.9 kpc) gives confidence that such counterparts may be found for other nearby events. As alluded to above, a definitive counterpart binary system has been associated to the ILT J1101 + 5521 system (Ruiter et al. 2024), harbouring an M-dwarf and WD in an orbit matching the 2.1 h periodicity of the radio emission. Most recently, the WD interpretation for minutes-long period transients has received support thanks to the recent detection in Hurley-Walker et al. (2024) of an optical counterpart for GLEAM-X J0704−37. The source is an M-dwarf with a very low chance of spatial coincidence thanks to the unusually high Galactic latitude of this system. Hurley-Walker et al. (2024) note that a stellar origin from a lone M-dwarf is unlikely, and they disfavour a M-dwarf–NS system, preferring an M-dwarf–WD binary. The binary nature of this system has since been conclusively identified by Rodriguez (2025), who found an orbital period matching that of the radio period (2.9 h), joining ILT J1101 + 5521 in this regard. The spectra reveal a comparatively massive WD companion to the M-dwarf in GLEAM-X J0704−37 at 0.8–1.0 $M_\odot$. Interestingly, renewed calibration of the source flux also significantly reduces the inferred distance of this source at ∼ 400 pc (Rodriguez 2025), in comparison to the original estimate of ∼ 1.5 kpc (Hurley-Walker et al. 2024).

For GLEAM-X J1627−52, deep X-ray observations have been able to place constraints on high-energy emission from the system (Rea et al. 2022), but the challenge of detecting a multiwavelength counterpart in the optical or NIR in its crowded location is compounded by a comparatively crude localization from the radio emission. Rea et al. (2022) obtained spectroscopy for three of the brighter candidate sources in the localization, finding them to be typical F, G, K stars, with no remarkable features.

Here, we present a comprehensive search for optical and NIR spectrophotometric variability in the vicinity of GLEAM-X J1627−52 as a means to identify candidate counterparts. Models detailed above place requirements on the nature of the optical counterparts stellar type and/or its existence in a tight binary configuration. Our data will be used to probe for the presence of peculiar stellar types, photometric variability, and radial velocity (RV) curves in sources local to GLEAM-X J1627−52, as a means to identify a candidate counterpart. Where appropriate, we assume a distance to the source of 1.3 ± 0.5 kpc based on its radio dispersion measure (Rea et al. 2022). In Section 2, we present our observations of the field of GLEAM-X J1627−52. We present our methods to search for an optical counterpart in Section 3 and our results in Section 4. These are discussed in Section 5.

2 OBSERVATIONS AND DATA REDUCTION

In order to probe any optical counterpart of GLEAM-X J1627−52, observations were acquired from three facilities of the European Southern Observatory (ESO) in Chile: the Multi Unit Spectroscopic Explorer (MUSE) mounted on UT4 of the 8.2-m Very Large Telescope (VLT), ULTRACAM mounted on the 3.5-m New Technology Telescope, and survey data from the 4.1-m Visible and Infrared

Downloaded from https://academic.oup.com/mnras/article/538/2/925/8029896 by guest on 26 March 2025

Table 1. OBs of MUSE data covering GLEAM-X J1627−52 as referred to in the text. Stacked epochs are composed as follows: OB1 [1–7], OB2 [8–14], OB3 [15–21], and all [1–6, 8–21].

Epoch name	Start time (UTC)	End time (UTC)	Exp time (s)
1	2022-05-25 06:31:32	2022-05-25 06:36:45	313.0
2	2022-05-25 06:38:47	2022-05-25 06:44:00	313.0
3	2022-05-25 06:46:02	2022-05-25 06:51:15	313.0
4	2022-05-25 06:53:16	2022-05-25 06:58:29	313.0
5	2022-05-25 07:00:29	2022-05-25 07:05:42	313.0
6	2022-05-25 07:07:44	2022-05-25 07:12:57	313.0
7	2022-05-25 07:15:00	2022-05-25 07:16:02	62.8
OB1	2022-05-25 06:31:32	2022-05-25 07:16:02	1940.8
8	2022-05-28 01:11:20	2022-05-28 01:16:33	313.0
9	2022-05-28 01:18:37	2022-05-28 01:23:50	313.0
10	2022-05-28 01:26:53	2022-05-28 01:32:06	313.0
11	2022-05-28 01:34:10	2022-05-28 01:39:23	313.0
12	2022-05-28 01:41:27	2022-05-28 01:46:40	313.0
13	2022-05-28 01:48:44	2022-05-28 01:53:57	313.0
14	2022-05-28 01:56:00	2022-05-28 02:01:13	313.0
OB2	2022-05-28 01:11:20	2022-05-28 02:01:13	2191.0
15	2022-05-28 02:06:40	2022-05-28 02:11:53	313.0
16	2022-05-28 02:13:54	2022-05-28 02:19:07	313.0
17	2022-05-28 02:21:12	2022-05-28 02:26:25	313.0
18	2022-05-28 02:28:27	2022-05-28 02:33:40	313.0
19	2022-05-28 02:35:40	2022-05-28 02:40:53	313.0
20	2022-05-28 02:42:56	2022-05-28 02:48:09	313.0
21	2022-05-28 02:50:12	2022-05-28 02:55:25	313.0
OB3	2022-05-28 02:06:40	2022-05-28 02:55:25	2191.0
All	2022-05-25 06:31:32	2022-05-28 02:55:25	6260.0

Survey Telescope for Astronomy (VISTA). Each of these data sets is described separately in the following sections.

2.1 VLT/MUSE

The MUSE instrument (Bacon et al. 2010) is an integral-field unit offering seeing-limited spatially resolved spectroscopy over a ∼1 arcmin field of view (FoV). This FoV comfortably covers the localization uncertainty (∼2 arcsec) of GLEAM-X J1627−52, and provides optical spectroscopy from 4800–9300 Å ($R \sim$ 1800–3600) across the field and so of every detected source. Observations were taken over three separate observing blocks (OBs) during late 2022 May. Each OB consisted of 7 × 313 s exposures with derotator offsets of 45 deg between subsequent exposures. The final exposure for the first OB was cut short to 62.8 s due to the approach of morning twilight. Details of these epochs are shown in Table 1.

Natural seeing was improved upon during observations through the use of a local tip-tilt star with the wide-field mode adaptive optics (AO) of MUSE. Although this AO mode causes a region of unusable data in the spectral region surrounding the Na I D doublet, this did not compromise any of the science goals of these data. No separate sky observations were obtained – instead spaxels void of astrophysical signal within the FoV were used for sky subtraction and calibration. Individual exposures within the OBs were reduced and then combined with the MUSE data reduction pipeline (Weilbacher et al. 2020, version 2.8.5) within the EsoReflex environment from ESO (Freudling et al. 2013). Sky residuals were further removed using the Zurich Atmospheric Purge (ZAP; Soto et al. 2016) software version 2.1 with default parameters. For input into ZAP, we constructed an aggressive source mask by calculating a sigma-clipped median and standard deviation, and flagging all pixels greater than one standard deviation above the median value. The 20 full-length exposures from all OBs (i.e. excluding the shortened final exposure of OB1, epoch 7) were also combined to generate a deep-stacked cube. In total therefore we have data cubes covering 25 'epochs' of MUSE observations: 21 numbered from the individual exposures, OB1, OB2, and OB3 from the stacked OBs and 1 'all' from the total exposure stack. Both individual exposures and the stacked OBs had full width at half-maximum measurements of 0.6–0.7 arcmin, as measured from bright stars in the field.

Spectra of sources within each data cube were extracted with the PAMPELMUSE software (Kamann, Wisotzki & Roth 2013; Kamann 2018). In the absence of a higher resolution image from which to build a source catalogue, as is typically done with PAMPELMUSE, and, given our field is not overly crowded, we instead built source catalogues directly from each MUSE epoch using a DAOPHOT (Stetson 1987) style star-finding algorithm to detect any source with a peak more than four times the background rms in white-light images formed from the cubes. PAMPELMUSE was then run using the recommended procedure and parameter choices,[1] to extract spectra at the location of each of these detections. The extraction process takes care of the changing position and shape of the point spread function throughout the spectral axis of the MUSE data cubes. As our initial source catalogue contains even marginal detections in the stacked cube, some sources could not have useful spectra extracted. The very low signal-to-noise ratio (SNR) of faint sources in short-wavelength ranges of the cube precluded the calculation of wavelength-dependent centroid and point spread function evolution by PAMPELMUSE. In practice, such marginal sources in our stacked cube would not allow for useful insights into their origin even if spectra were extracted.

An absolute world coordinate solution (WCS) solution is not performed during ESO data reduction of MUSE data and is instead populated by the telescope pointing coordinates which may be inaccurate by a few arcseconds. Therefore, to accurately cross-match sources detected in individual epoch catalogues we tied each data cube's WCS to that of a Dark Energy Camera (DECam; Flaugher et al. 2015) image accessed via the NOIRLab archive.[2] The alignments were done using SPALIPY (Lyman 2021) to calculate and perform source-based affine transformation of the MUSE data onto the pixel space of the DECam image. Alignment residuals were ∼ 0.4–0.5 MUSE pixels (∼0.1 arcsec). This is much smaller than our source density and allowed unambiguous source matching between catalogues. This also allowed us to place the sources on an accurate absolute WCS plane for locating GLEAM-X J1627−52 and searching within its localization uncertainty. Due to varying data quality, each source was not able to be extracted from every epoch. Each unique source was assigned an arbitrary ID based on ascending declination, which will be referred to in later sections.

2.2 NTT/ULTRACAM

ULTRACAM is a high-speed, triple-beam imaging photometer (Dhillon et al. 2007). A total of 682 frames of GLEAM-X J1627−52 were obtained with ULTRACAM on 2022 March 4, each composed of three images taken simultaneously in the super Sloan Digital Sky Survey (SDSS) filters $u_s g_s i_s$ (Dhillon et al. 2021). The instrument

[1]Using documentation contained within https://gitlab.gwdg.de/skamann/pampelmuse/.
[2]https://astroarchive.noirlab.edu/

Downloaded from https://academic.oup.com/mnras/article/538/2/925/8029896 by guest on 26 March 2025

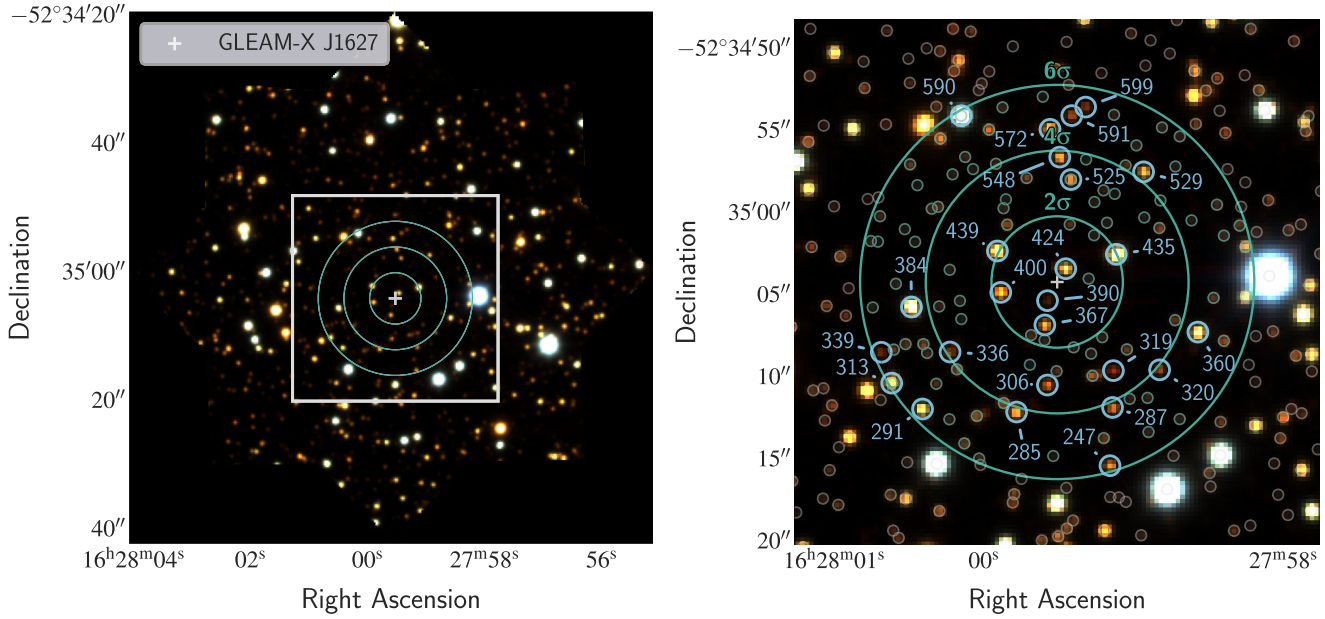

Figure 1. The FoV and sources detected in the MUSE data in the vicinity of GLEAM-X J1627−52 (central white cross). The pseudo-colour image was generated by collapsing the data cube in three wavelength ranges. The right panel is a zoom-in of the left (extent indicated by white box on left panel), and highlights individual sources detected by our algorithm with circle markers. The extent of the 2σ, 4σ, and 6σ location uncertainties on GLEAM-X J1627−52 (where $\sigma \simeq 2$ arcsec) are shown with larger, labelled cyan circles, and sources within 6σ have their circle markers coloured differently. Sources referred to throughout in text and figures, and those matched with a *Gaia* source, are labelled with IDs. These are arbitrary, and designated in ascending declination order from the entire MUSE cube source catalogue. The effect of 45 deg rotations between exposures gives the FoV shown on the left as an the eight-pointed star shape.

was used in its two-windowed, unbinned mode, with 10 s exposure times and 0.024 s dead time between each frame. The sky was photometric with seeing of approximately 1 arcmin and no Moon.

The ULTRACAM data were reduced using the HiPERCAM aperture photometry pipeline (Dhillon et al. 2021). All frames were first debiased and then flat-fielded, the latter using the median of twilight sky frames taken with the telescope spiralling. We then shift-and-added all 682 frames to produce a deep image in each filter from which we identified 14 significant sources that fall within 12 arcsec (6σ localization) of GLEAM-X J1627−52.

2.3 VISTA

The footprint of the VISTA Variables in the Via Lactea (VVV) public survey (Minniti et al. 2010) taken on VISTA telescope serendipitously contains the localization of GLEAM-X J1627−52. We obtained all available VISTA/VVV K_s-band imaging covering the location of GLEAM-X J1627−52 from the ESO science portal.[3] These data are available pre-reduced (for details, see Cross et al. 2012) and contain 99 epochs, covering a time-span from 2016 July 11 until 2019 September 1. Unfortunately, none of these data cover the period of radio activity during early 2018.

Although the baseline from early VVV epochs to our MUSE data could in principle be used to search for proper motion sources, it would require a relative astrometric accuracy of $\lesssim 0.2$ arcsec to probe even high Galactic transverse velocities (hundreds of km s^{-1}). Achieving this requirement is compromised by having only very few bright, isolated sources in both MUSE and VVV FoV, alongside differences in wavelength coverage and the variable quality point spread function of the VVV data.

[3]https://archive.eso.org/scienceportal/home

3 METHODS

To investigate possible counterparts to GLEAM-X J1627−52, we applied a number of methods of investigation to sources in the vicinity. For the remainder of the paper, unless otherwise stated, we will concentrate our analyses and discussion on those sources located within the 6σ localization uncertainty of GLEAM-X J1627−52 – i.e. those sources highlighted in Fig. 1. A radius encircling 6σ of the localization was chosen to be conservative to the presence of under-estimated uncertainties, or systematics, in the radio localization.

3.1 Photometric variability

3.1.1 NTT/ULTRACAM

We performed photometry using normal and optimal (Naylor 1998) extraction of the 14 sources we identified, using both fixed-radius apertures and apertures that varied in radius with the seeing. The location of the sources are identified on Fig. 1 and detailed in Appendix A. We note two ULTRACAM sources (identified as IDs 287 and 548) have comparable brightness sources in the vicinity, and were seen as blended sources. For these an aperture was used for these sources that also included flux from the neighbouring sources.

We searched for periodicities in all sources using both Lomb–Scargle (Press & Rybicki 1989) and phase-dispersion minimization (Stellingwerf 1978) periodograms, the latter technique being particularly sensitive to highly non-sinusoidal signals in the optical light curves, following the methodology of Dhillon et al. (2011).

Downloaded from https://academic.oup.com/mnras/article/538/2/925/8029896 by guest on 26 March 2025

3.1.2 VISTA/VVV

We performed aperture photometry with the PHOTUTILS (Bradley et al. 2024) package on 14 detected objects within the 6σ localization of GLEAM-X J1627−52 – the sources are detailed in Appendix A and indicated on Fig. 1 (all were matched within ∼0.5 arcsec of their respective MUSE source). We obtained Two Micron All Sky Survey (2MASS; Skrutskie et al. 2006) K_s-band magnitudes of comparison stars in each image to determine the zero-point and its uncertainty. After calibrating our photometry using the zero-point, we constructed light curves for each source, retaining those detections with an SNR of at least three. Given the typical depth of a VVV image, all photometric measurements of the 14 sources was comparatively low SNR. For this reason, we first employed quick quality checks on the overall data to ascertain if it was conducive to more rigourous searching for variability. Each light curve was fitted with a simple constant and linear-in-time model to search for long-term evolution. The residuals around each of these models were then checked to determine the presence of residuals not dictated purely by statistical noise. As will be shown in Section 4.1, these results indicated no meaningful departure from constant evolution, and so we forewent further analysis of these data.

3.2 Spectral typing and emission line search

MUSE data allow us to make a flux-limited census of the stellar sources in the vicinity of GLEAM-X J1627−52. We use this to search for either spectral peculiarities in sources, or any systems matching theoretical expectations for the counterpart system.

In order to guide our search, we made use of PYHAMMER (version 2.0.0; Kesseli et al. 2017; Roulston, Green & Kesseli 2020) to automatically classify sources based on its own spectral template library. It additionally allowed us to visually inspect the template match for each of our source spectra – extracted from the deep-stacked data cube – and update the classification manually. A detailed typing was not the aim of our investigations, but rather we used the library of templates to help with broad stellar typing and anomaly detection. This method was performed for all sources within the 6σ localization of GLEAM-X J1627−52. Prior to ingestion into PYHAMMER, we applied an SNR per spectral pixel cut on the spectra of 8 using the PYHAMMER configuration interface.

We concentrated a search for emissions lines, and any variability in emission lines between MUSE epochs, around the Hα region of the spectra. Hα is one of the strongest lines and is readily excited, giving the best possibility to observe unusual macroscopic conditions of any counterpart system – e.g. Hα is not typically excited in the atmospheres of low-mass stars (although can be present during flares and heightened activity), but has been seen to be prominent in close WD binary systems, such as the WD pulsar systems, as a result of interaction or accretion processes. For this search, the OB1, OB2, and OB3 MUSE epochs, were passed through synthetic top-hat narrow-band filter profiles: a Hα filter centred on 6563 Å with a width of 200 km s^{-1}, and a continuum filter located +12 Å relative to the Hα filter. A width of 200 km s^{-1} was chosen to comfortably capture any reasonable Doppler shifts of putative emission and the instrumental broadening of the line in MUSE data, whilst not acquiring too much added sky noise. The continuum-subtracted Hα filter flux was used to search first for significant Hα emission across the entire FoV, and secondly to quantify the significance of variability in the Hα region between the epochs. During construction of these synthetic narrow-band images, we employed the method detailed in Fossati et al. (2019) and Lofthouse et al. (2020) to correctly estimate variances. Succinctly, the distribution of values in sky pixels (i.e. those not flagged by our source mask used in the ZAP reduction process) divided by σ are expected to be normal, with a scale factor of 1. σ is calculated by propagating the pixel variances in the STAT extension of the MUSE data for the narrow-band image creation process. In each case, a factor 2.4–2.5 needed to be applied to the naïve σ values to satisfy this condition.

3.3 Radial velocity variability

Many leading scenarios for GLEAM-X J1627−52 invoke a close binary systems containing an NS or WD. We may expect to detect such a system in our multi-epoch MUSE data as a variation in the RV of a source. Based on our results of spectral typing of the sources in the vicinity of GLEAM-X J1627−52 (see Section 3.2), along with the typical low SNR of our spectra, we opted to perform a full template fitting of the spectra using the SPEXXY[4] package (e.g. Husser et al. 2016), along with PHOENIX-ACES stellar model library (Husser et al. 2013) with $T_{\rm eff} = 2300 - 15000$ K, interpolated to match the resolution and the line spread function of MUSE. The template-fitting was performed for all epochs for each source. The mid-times of our MUSE epochs were corrected to Barycentric Dynamical Time to act as the timestamps for our RV measurements.

The MUSE instrument, in terms of wavelength-calibration (equivalently velocity accuracy) of the final data cubes, has been characterized to ~ 1 km s^{-1} over most of its wavelength coverage. However, a position-dependent shift at the level of 2.5–4.0 km s^{-1} for individual lines exists (Weilbacher et al. 2020). Our observing strategy rotates and dithers the instrument between subsequent epochs (to alleviate detector artefacts in our stacked cubes). As such this source uncertainty manifests as another source of pseudo-random uncertainty on velocity values. We therefore add a 3.25 km s^{-1} uncertainty (as the mid-point of the position-dependent uncertainty) in quadrature to our statistical uncertainty from the template fitting. Although strategies exist to mitigate this position uncertainty, and recover the instrument accuracy (e.g. Kamann et al. 2016), the typical level of variability we are expecting for all but pathologically inclined systems (See Section 5) would anyway dominate over this uncertainty, and so we did not include such corrections as they are not expected to impact our results.

For sources where SPEXXY fitting was successful for at least five individual epochs, resultant RV evolution was modelled separately as a sinusoid and as a constant (i.e. a systematic offset with no evolution). The Bayesian likelihood of model parameters were explored using the nested sampling Monte Carlo algorithm MLFriends (Buchner 2016, 2019), implemented in the ULTRANEST package (Buchner 2021) and using a Gaussian log-likelihood function. The prior on the sinusoid period was $P_{\rm orb} \sim U(15, 300)$ min to comfortably capture both the measured period of GLEAM-X J1627−52 at 18.18 min (Hurley-Walker et al. 2022) and the expected orbital periods of close WD binary systems. Although the expectation is that the radio emission period is not related to the binary orbit (and would be more likely the spin period of a binary constituent), we opt for this wide orbital period prior to elucidate any potentially interesting systems – an NS harbouring system could be in a much tighter orbital configuration, for example. The semi-amplitude and systematic offset priors were $K_2 \sim U(0, 900)$ km s^{-1} and $\gamma \sim U(-600, 600)$ km s^{-1}, respectively to, again, comfortably encompass any potential system. The same systematic offset prior was used for the constant model.

[4] https://github.com/thusser/spexxy

Downloaded from https://academic.oup.com/mnras/article/538/2/925/8029896 by guest on 26 March 2025

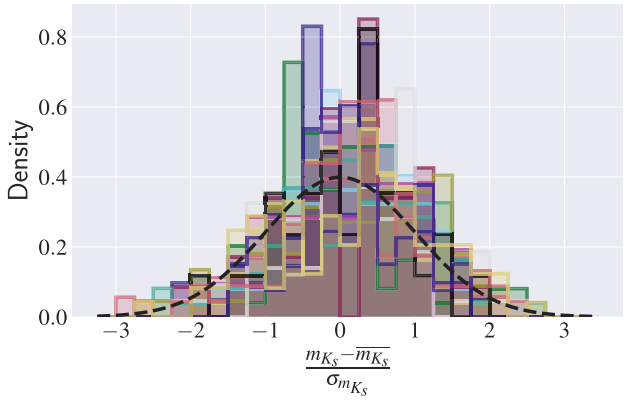

Figure 2. Sigma-normalized residuals of individual K_s-band photometry detections from a constant model ($\bar{m_{K_s}}$) in the light curves of the five VISTA/VVV sources investigated. The lack of significant deviation beyond that expected from statistical noise (i.e. a normal distribution centred on zero with a standard deviation of one, indicated by the black dashed line) from the constant model indicates consistency with the model and the inadequacy of the data to perform more detailed searches of periodic behaviour.

Although baseline and coverage of our MUSE data are not ideal for a robust search for $P_{\rm orb}$ on time-scales of hours, such systems should have K_2 values of hundreds of $\rm km\,s^{-1}$ (e.g. Marsh et al. 2016), meaning a modelled search combined with visual inspection would reveal these readily in our data. There is, however, always the potential for binary-plane inclination to diminish the expected amplitude.

We finally note that individual MUSE exposure data cubes are susceptible to significant artefacts, brought on by the image slicing instrumentation configuration. Although typically mitigated by stacking of exposures, here it adds an additional source of variable noise within the individual epochs. This accounts for some individually discrepant points, and the variable precision of the RV measurements within a pointing. This also did not allow simple statistical cuts (e.g. on χ^2/dof) to be trusted at face value, and we instead relied on manual inspection alongside our sinusoid fitting procedure.

4 RESULTS

In Fig. 1, we indicate IDs for specific sources that were further investigated or are referred to individually in the following section.

4.1 Photometric variability

In Fig. 2, we plot the residuals of individual photometric detections in our VISTA/VVV source light curves from the constant model. All data points for each source are consistent with being distributed around a constant model within the uncertainties of the photometry, therefore precluding a deeper investigation into the nature of any variability of the sources. Fits using a linear-in-time model for the light curves gave slopes broadly consistent with no evolution, given the accuracy of the data. Much deeper NIR data will be required to place meaningful constraints on the nature of any variability in this regime.

We additionally found no evidence for periodic or other variability (via manual inspection) in any of the 14 ULTRACAM sources within (6σ) localization of GLEAM-X J1627−52.

4.2 Spectral typing and emission line search

The majority of spectra precluded even broad stellar typing owing to relatively low SNR. For ∼70 per cent of sources, neither the spectral match provided initially by PyHammer, nor manual inspection, provided a reasonable match. These sources were typically red continua with an absence of features (at the level of our data quality), although there are a small number of brighter sources with more clearly featureless red continuum spectra. For those sources where typing was possible, the population consists of predominantly early M-dwarfs and late K- or G-type stars. Three spectra of bright stars in the vicinity were presented by Rea et al. (2022), these are source IDs 424, 400, and 439, labelled by those authors G1, G3, and G4, respectively. We confirm comparable spectral typing and the absence of distinguishing features, as noted by Rea et al. (2022), for these sources. Importantly for the model of Loeb & Maoz (2022), we find no indications of a hot subdwarf local to GLEAM-X J1627−52 – i.e. no source spectra displays a blue continuum with strong H absorption lines. Any such hot subdwarf at a distance of ~ 1.3 kpc would be well detected in our data (see Section 5).

Even the brightest WDs would have an apparent visual magnitude of $\gtrsim 21$ mag at the distance of GLEAM-X J1627−52, with more typical WDs being $\sim 22-24$ mag (Gentile Fusillo et al. 2021). As such the prospects of directly identifying any WD counterpart spectroscopically in our MUSE data is limited. This issue is compounded by the fact that any viable WD counterpart candidate system would be in a tight binary system (Katz 2022, although see Rea et al. 2024) and so is likely to be outshone significantly at our wavelength coverage ($\gtrsim 4800$ Å) by its non-degenerate companion. This is also demonstrated in Hurley-Walker et al. (2024), where optical spectra of the M3V optical counterpart for a comparable distance long-period radio transient (GLEAM-X J0704−37) precludes detection of a companion WD with similar wavelength coverage. The lack of a spectral-typed WD from the data did not therefore strongly constrain the presence of a WD in the localization region of GLEAM-X J1627−52, which is better probed by variability information (Sections 4.1 and 4.3), as well as the presence of peculiar spectral features in a companion.

Using continuum-subtracted Hα narrow-band images we found no significant variability of any source within the 6σ localization of GLEAM-X J1627−52 – the most significant individual pixel in this region shows a variability of $\sim 3\sigma$ in flux, with no signs of an astrophysical source undergoing variation. Fig. 3 shows the significance of spaxel variability in the Hα spectral regime. For the three prominent sources outside the localization of GLEAM-X J1627−52 we see no evidence of particularly unusual behaviour, and indeed, given they are the three brightest sources in the field, ascribe the variation seen as due to flux-calibration uncertainties.

Following a search for variable Hα emission, a visual inspection of a mean continuum-subtracted Hα image (formed from those of OB1, OB2, and OB3) highlighted two point sources of emission in the vicinity of GLEAM-X J1627−52: source IDs 319 and 339. The source spectra display clear unresolved Hα emission and, in the case of source ID 319, Hβ emission (Fig. 4). A comparison of the stellar spectrum with stellar templates from the ESO MUSE Stellar Library (Ivanov et al. 2019) and the Pickles Stellar Library (Pickles 1998) was performed, indicating they are approximately M5–M6 type stars, which was also corroborated by our initial PyHammer typing. Radio emitting close WD binary systems such as AR Sco (Marsh et al. 2016) and J191213.72−441045.1 (Pelisoli et al. 2023), display prolific Hα in emission on top of an M-dwarf spectrum, due to irradiation of the WD companion in each system. However,

Downloaded from https://academic.oup.com/mnras/article/538/2/925/8029896 by guest on 26 March 2025

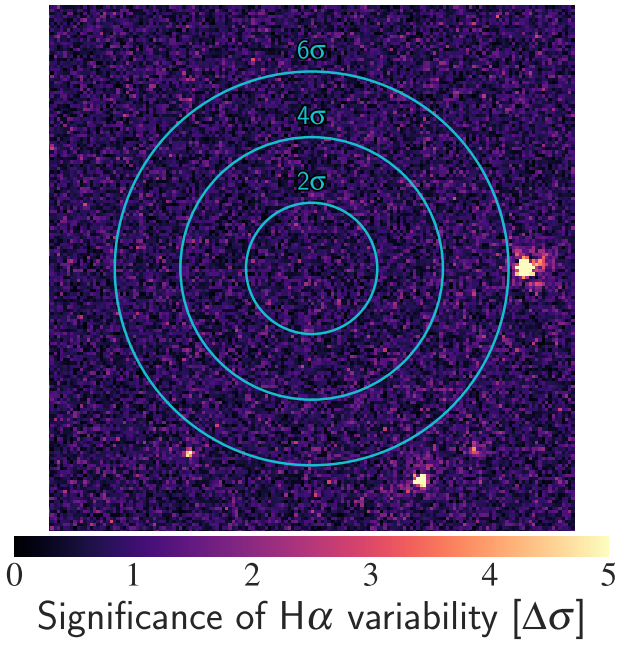

Figure 3. The maximal variation of Hα emission between the three OB-stacked MUSE cubes, expressed as a sigma value – i.e. the significance of Hα variability – with localization contours of GLEAM-X J1627−52 overlaid. No significantly varying source is found within 6σ of GLEAM-X J1627−52. Sources around the edge of the frame are residuals from very bright stars owing to imperfect flux calibration.

other non-binary mechanisms for Hα emission in M-dwarfs are also possible, as discussed later.

The equivalent width (EW) of Hα emission for source IDs 319 and 339 are given in Table 2 for each of our combined epochs. There is no evidence for variation in the Hα strength for a given source.

Table 2. Hα EWs for the two emission lines sources in the vicinity of GLEAM-X J1627−52 along with their weighted mean over the three epochs. Values are in Å.

ID	OB1	OB2	OB3	Mean
319	-5.2 ± 0.7	-7.4 ± 0.8	-5.9 ± 0.8	-6.1 ± 0.4
339	-4.8 ± 0.8	-3.1 ± 0.9	-3.6 ± 1.0	-3.9 ± 0.5

4.3 Radial velocity variability

Following the method detailed in Section 3.3, there were 78 sources in the 6σ region of GLEAM-X J1627−52 for which we could compute sinusoid and constant model parameter posteriors. These models were visually inspected for each source. Sources were discarded that had either (i) a Bayes Factor indicating no strong preference for the sinusoid model over a constant evolution, (ii) no well-determined period and amplitude, (iii) discrepant individual measurements driving the posteriors or (iv) RV measurements from the OB1, OB2, and OB3 epoch spectra that were not representative of the mean of the individual epoch RVs for each – this latter check was effective to discriminate against low SNR spectra for which variations in individual epochs were driven by the limitations of the template fitting technique. Sources that pass these inspection criteria are shown in Figs 5 and 6.

Each source displays some form of variability that appears inconsistent with no evolution (i.e. the constant model), although in cases the sinusoid fits also do not present a convincing description of the data. Three sources (IDs 295, 348, and 359; Fig. 5) have solutions favouring $P_{\rm orb} \lesssim 0.4$ h. If these were to be real, they would be tight binaries in the regime of compact binaries, and would additionally require very low orbital inclination to explain the comparatively low semi-amplitude of the sinusoid (see Section 5). For three other sources (IDs 468, 526, and 548; Fig. 6) we find $P_{\rm orb} \sim 2, 1, 4.5$ h, respectively. Sources 526 and 548 are comparatively bright, and yet their RV curves appear erratic with respect to the sinusoid model. Similarly to sources fitted with shorter periods, the semi-amplitudes seen are low compared to that expected for realistic binary configurations in all but low orbital inclination systems. As

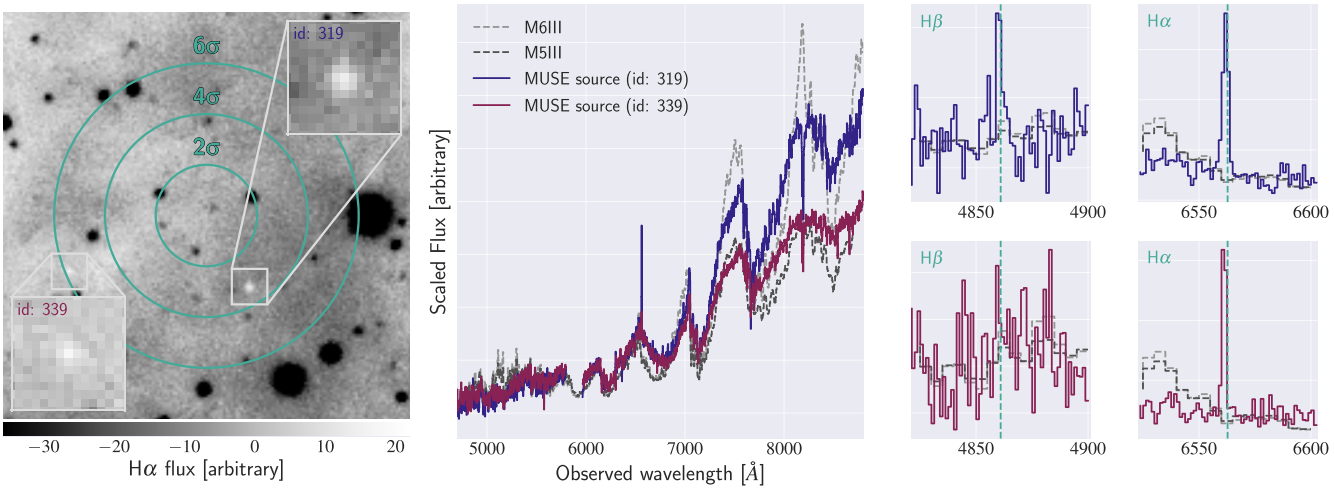

Figure 4. Left: the mean Hα narrow-band emission image from OB1, OB2, and OB3 MUSE epochs. Two sources are seen in emission, approximately 3.2σ and 6.0σ from the localization of GLEAM-X J1627−52. Centre: the spectra from the 'all' MUSE epoch of the emission sources. Shown in comparison are spectra of M5III and M6III stars (Pickles 1998). Spectra were normalized to the same median flux level in the 4800 − 6800 Å wavelength range. Right: a close-up of the Hα and Hβ regions of the spectra, with the MUSE source spectra shown on different subplots for clarity. The RV of these sources revealed no evidence for a short-period binary configuration (see Section 4.3).

Downloaded from https://academic.oup.com/mnras/article/538/2/925/8029896 by guest on 26 March 2025

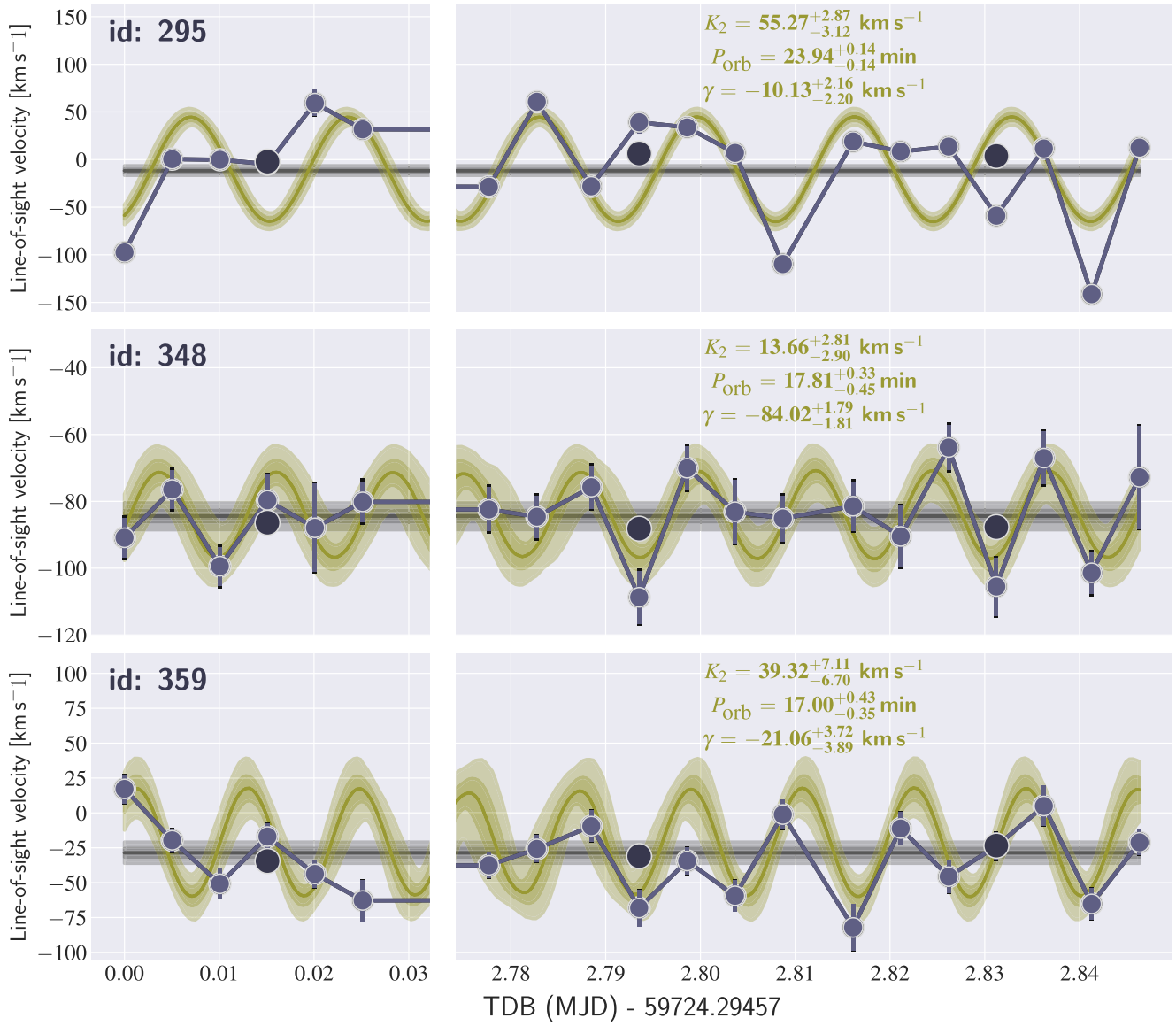

Figure 5. RV measurements for sources passing our initial vetting cuts for sinusoidal fitting. We show these sources as the examples with a closest approximation to a tight binary signature expected from many models of GLEAM-X J1627−52. However, we make no strong claims on their reality as such systems owing to: the poor description of the data by the sinusoid in some cases, the possibility of underestimated/unaccounted for uncertainties on individual measurements, and the astrophysical implications of such detections (see the text). Measurements from individual MUSE epochs are shown as lighter circle markers, joined by solid lines, with larger, darker markers indicating the measurements from the combined epochs OB1, OB2, and OB3. Bars on each marker show the statistical uncertainty from SPEXXY alone, and for the increased error budget including instrumental effects in black (see Section 3.3), although not always visible. On each subplot, the median posterior models are shown by thick lines in green and grey for the sinusoid and constant models, respectively. The P_{16-84} and P_{1-99} percentile regions for each model are shown by the shaded regions. Sinusoid parameters are given as the median and P_{16-84} percentile interval. Locations of sources (based on their ID) are indicated on Fig. 1.

elaborated further in Section 5, although the variations in RV do not appear to be simply systematic variations between epochs for the different sources, we do not consider the above six systems as strong binary candidates due to astrophysical considerations, not least because of the huge inferred spatial density of such systems. In terms of localization, source IDs 359 and 468 are within the 2σ localization of GLEAM-X J1627−52. Where determined, the RV curves of the other sources within 2σ of GLEAM-X J1627−52 are additionally shown in Appendix B.

We further analysed the two emission line sources identified in Section 4.2 by comparing the RVs from the SPEXXY template-fitting package to characterize the M-dwarf stellar spectrum, with that of an emission line fit to Hα. The fit to Hα was done using a single Gaussian and a third-order Legendre polynomial for the local continuum. Sampling of the posterior distributions used a similar ULTRANEST procedure as used for the RV modelling (Section 3.3). The results are shown in Fig. 7. For source ID 319, no RV variation is found, whereas formally the sampling determines a low-amplitude, short period for source ID 339 but with no well-defined phase. As above, for reasons discussed in Section 5, we do not consider this RV evolution to be indicative of expected counterpart behaviour. Noticeably, there appears to be an offset between the line-of-sight

Downloaded from https://academic.oup.com/mnras/article/538/2/925/8029896 by guest on 26 March 2025

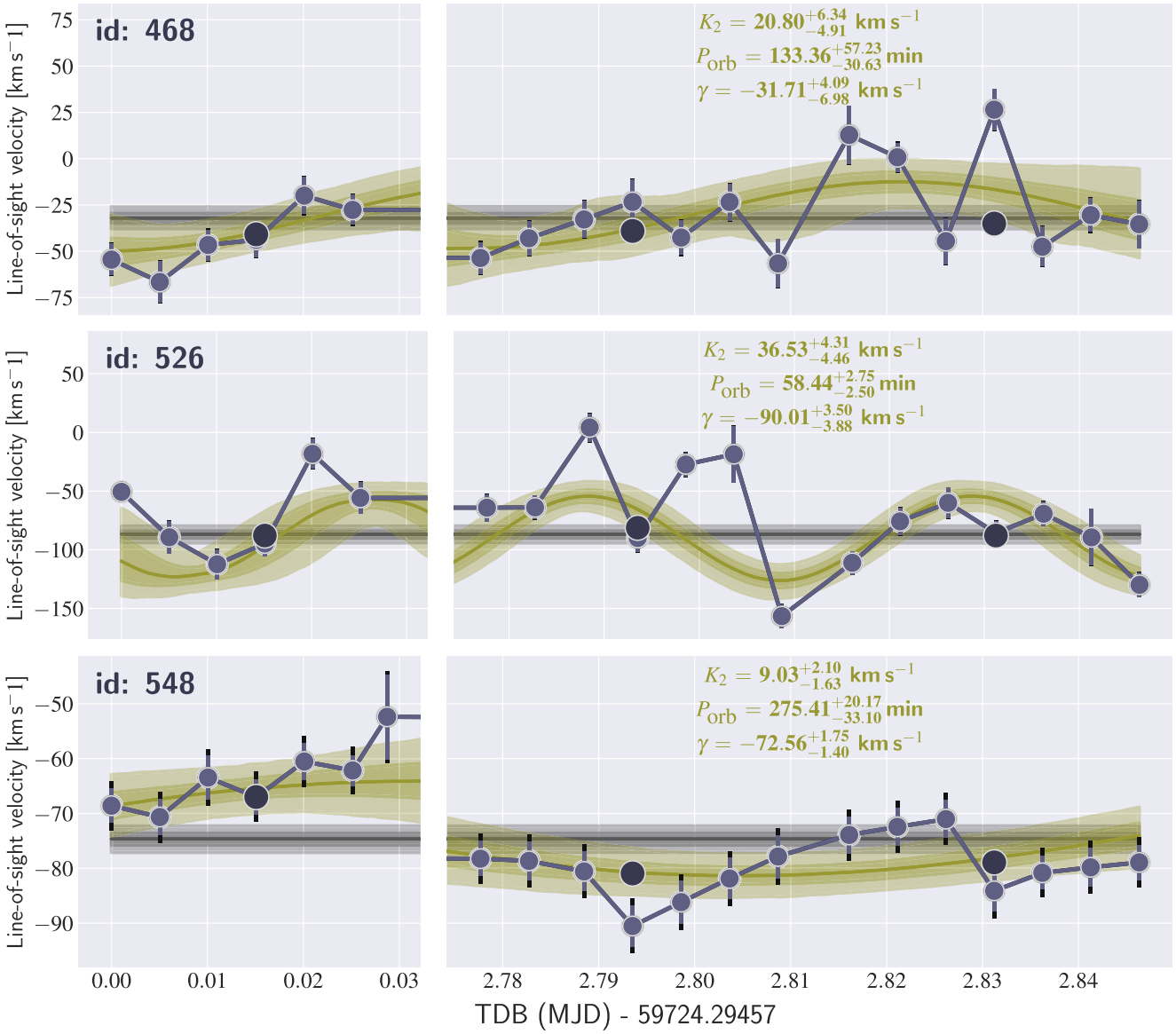

Figure 6. Same as Fig. 5, but here shown for three other sources with model fits alluding to longer RV periodicity.

velocity determined from the template-fitting and the Hα emission line fit. Line emission in binary systems may arise from geometrically distinct locations compared to the centre of light and so be offset in velocity. In isolated M-dwarfs, it would require a localized region of emission in order to show such an offset, but in this case we would also expect its velocity offset to change with time due to stellar rotation. As the level and direction of offset is similar and unchanging between the two sources, we conclude it is unlikely to be astrophysical in origin. Although the underlying reason for this remained uncertain after investigation,[5] the constant offset with epoch in each suggests the emission is arising from the star in each case.

[5]A comparison of the velocities of Hα absorption, determined equivalently, and SPEXXY template fits for the bright source ID 435 did not show this systematic offset.

5 DISCUSSION

The location of GLEAM-X J1627−52 is in a dense region of the Galactic plane. Our stellar typing using MUSE spectra of sources in the localization showed the population to be composed primarily of low-mass main-sequence stars, as is to be expected. Within this population we found no evidence of isolated WDs or hot subdwarf stars. In order to quantify our sensitivity to such sources we performed a photometric analysis of our MUSE data. The wavelength coverage of MUSE is comparable to the *Gaia G* band, excepting a lack of coverage from 4000 − 4700 Å. We built a white-light image from our 'all' epoch and cross-matched aperture photometry of sources detected using SEP (Barbary 2018, itself built on the algorithm of Bertin & Arnouts 1996) with the *Gaia* Data Release 3 (Gaia Collaboration 2023) catalogue, accessed via ASTROQUERY (Ginsburg et al. 2019). From this, we estimate a zero point of 28.1 mag and a 5σ limiting magnitude of 24.4 mag in the white light image. Spectral typing was possible $\sim$ 1 mag brighter than this

Downloaded from https://academic.oup.com/mnras/article/538/2/925/8029896 by guest on 26 March 2025

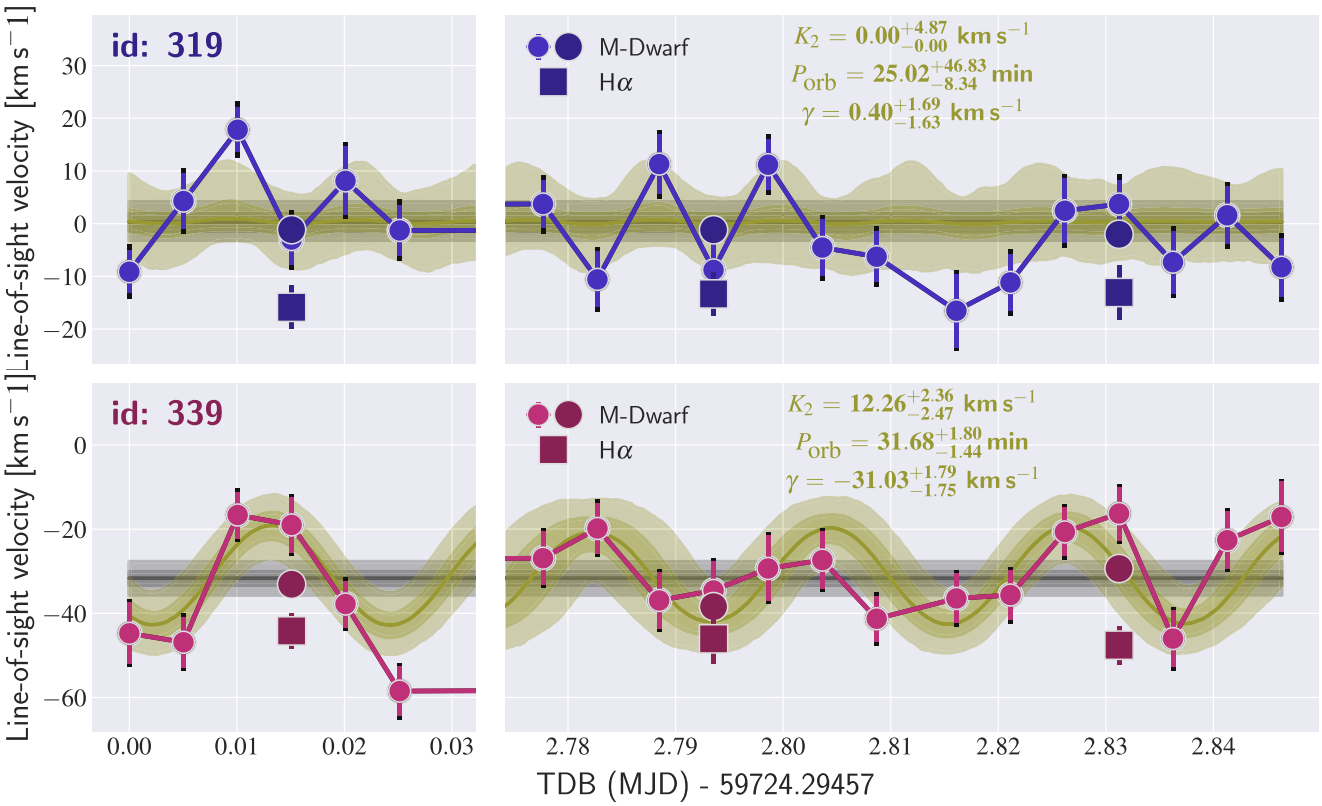

Figure 7. Same as Fig. 5, but here for two emission line sources identified in Section 4.2 and shown in Fig. 4. Neither show strong evidence for RV variation and such low $P_{\rm orb}$ values as favoured by our posterior sampling are unrealistic for a binary containing a non-degenerate star. Also shown is the RV of the Hα emission lines are show for the combined OB1, OB2, and OB3 epochs as large square markers. Sources are colour-coded the same as Fig. 4.

limit at the level of identifying the spectral continuum shape. As discussed in Section 4.2, WDs are expected to be $\sim 22-24$ mag at the distance of GLEAM-X J1627−52. Therefore, although we would expect to have been able to highlight WD candidates based on a blue-continuum slope, we would not expect to make a robust classification. Nevertheless, as shown in Appendix B, no detected source within 2σ of the localization shows any characteristics of a WD considering the expected modest extinction along the line of sight to GLEAM-X J1627−52. Should the distance to GLEAM-X J1627−52 be revised significantly downwards, as was the case for GLEAM-X J0704−37 (Rodriguez 2025), our limits become more constraining on the presence of a WD, although any significant revision in distance is likely to require a multiwavelength counterpart in the first place. Unlike WDs, however, hot subdwarf stars are comparatively bright in optical – $M_G \sim 2-7$ mag (Culpan et al. 2022). This would mean the faintest would appear at $m_G \sim 17.5$ mag even at the upper distance estimate for GLEAM-X J1627−52. As such we rule out the presence of a counterpart matching the expectations of Loeb & Maoz (2022). The presented data also constrain short- and long-time-scale brightness changes (ULTRACAM and VVV, respectively) for the brighter sources in the localization, whereas variability has been seen in counterparts to other long-period radio sources (e.g. Pelisoli et al. 2023).

Close binary systems including a WD provide us with additional plausible counterpart systems to the radio emission given such systems display indicators of the close interaction between a WD and a non-degenerate companion in the form of emission lines. Although we identified no variable Hα emission, two point sources of constant Hα emission were identified (source IDs 319 and 339, Fig. 4). The configuration of their spectra is reminiscent of the known WD pulsars (Marsh et al. 2016; Pelisoli et al. 2023) – namely Balmer emission superposed on a mid M-dwarf spectrum. In the case of WD pulsars, the Balmer emission is seen to be both strong and variable – Hα EW varying from tens to > 100 Å across their orbital phase (Garnavich et al. 2019; Pelisoli et al. 2023) – due to WD-irradiation of a face of the M-dwarf. Indeed, even for detached (non-interacting) close M-dwarf–WD systems, such irradiation produces strong Balmer emission (Marsh & Duck 1996), unless the WD is very cool. Our results show no strong evidence of variability in the Hα EW of our sources (Table 2), and in any case they are at a much lower level (< 10 Å). Also unlike the WD pulsars' spectra, we did not detect helium emission in our sources. (A search at the strongest optical transition, He Iλ5876 Å, was compromised due to the notch cut from our spectra by the Na D guide laser on MUSE, however.) Balmer emission in M-dwarfs can however be produced by isolated stars due chromospheric activity. The characteristics of this emission, and particularly its relation to the rotation period of the star, at least up to the point of saturation, points to a magnetic dynamo origin (e.g. Reiners, Joshi & Goldman 2012; Newton et al. 2017; Ibañez Bustos et al. 2023, and references therein). Our Hα EW measurements are well within the expectations of M-dwarf activity (Newton et al. 2017; Kumar et al. 2023). These sources also display no strong RV periodicity indicative of a close binary system (Fig. 7), which should have a significant amplitude except for face-on systems. Finally, our spectra of the sources do not show any blue-continuum contribution above that expected from the M-dwarf template (Fig. 4). Such a slope would be indicative of the presence of a WD, although we reiterate our MUSE data are only sensitive to the relatively luminous WDs at

Downloaded from https://academic.oup.com/mnras/article/538/2/925/8029896 by guest on 26 March 2025

the distance of GLEAM-X J1627−52 and in any case do not extend to sufficiently blue wavelengths where a WD would contribute most flux to the system. For the above reasons, we do not ascribe either of these emission sources as being credible counterparts on the available information.

Plausible systems for GLEAM-X J1627−52 and other long-period radio transients are close binary systems. Although how (or whether) the period of radio emission relates to the orbital period of each system can be less clear. The recently discovered ILT J1101 + 5521 system (Ruiter et al. 2024) has shown radio emission can occur on the orbital period of a system (likely due to magnetic locking of the rotation of the WD), but the radio period in that case is ~ 2 h. In other systems with radio periodicities of minutes and identified counterparts, the period is linked to the spin of the degenerate companion (Marsh et al. 2016; Pelisoli et al. 2023), while the systems are in a binary orbit with $P_{\rm orb} \sim$ hours. The 18.18 min radio period seen for GLEAM-X J1627−52 is not expected to be directly related to a binary orbit involving a WD or NS and a non-degenerate companion (the companions our data are sensitive to), as such a system would not be stable. Succinctly, any plausible system with an orbital period at the radio period of GLEAM-X J1627−52 would require a compact binary system (WD/NS + WD/NS), which are beyond the sensitivity of our data for RV analysis. We preface the next discussions on our RV analysis by emphasizing we do not find any convincing signature of a short-period binary system and so no strong counterpart candidate, but provide a full discussion for completeness.

Our search for sinusoidal RV behaviour, indicative of a binary system, confirmed no source provides a convincing candidate with $P_{\rm orb} \lesssim 0.5$ h, in line with astrophysical arguments above. What variability was seen has semi-amplitudes of $\lesssim 55$ km s^{-1}. We can constrain the expected amplitudes of RV variability with typical expected binary configurations using the binary mass function:

$$\frac{(M_2 \sin i)^3}{(M_1 + M_2)^2} = \frac{P_{\rm orb} K_2^3}{2\pi G}, \quad (1)$$

where M_1 and M_2 are the seen and unseen component masses respectively, i is the orbital inclination, $P_{\rm orb}$ is the orbital period, K_2 is the RV semi-amplitude, and G the gravitational constant. This is shown in Fig. 8 for a modest inclination of $i = 5$ deg. At a very modest orbital inclination of 5 deg, any unseen component mass typical of an NS ($\gtrsim 1.0\,M_\odot$) would produce a RV semi-amplitude of ~ 50 km s^{-1} at $P_{\rm orb} = 0.5$ hour. Although comparable to the amplitude seen for source ID 296 (Fig. 5), as mentioned, such a short period is in any case not expected to be stable for a non-degenerate companion. Additionally the RV variation is not convincingly sinusoidal, and the source being 4σ from GLEAM-X J1627−52. Although source ID 359 is within 2σ of the localization, it would require a low-mass NS in a pathologically inclined orbit, even notwithstanding that the inferred $P_{\rm orb}$ is unrealistic for a stable system. Our search for evidence of longer period sources with $P_{\rm orb} \sim$ hours, as shown in Fig. 6, again revealed no convincing candidate. What RV amplitudes are favoured by the posterior sampling is at very low amplitudes, similarly requiring very low orbital inclination systems. We further note other sources of RV variability could be contributing that are unaccounted for, in particular stellar activity can reach imprints of several km s^{-1} for the typical mid-type M-dwarf, reach above 10 km s^{-1} for late-types (Jenkins et al. 2009).

Low-mass stellar companions with a typical $\sim 0.6\,M_\odot$ WD companion offer some more flexibility with respect to plausible inclinations. On the balance of proximity and data quality, source ID 468 perhaps best approximates to the signature one would expect,

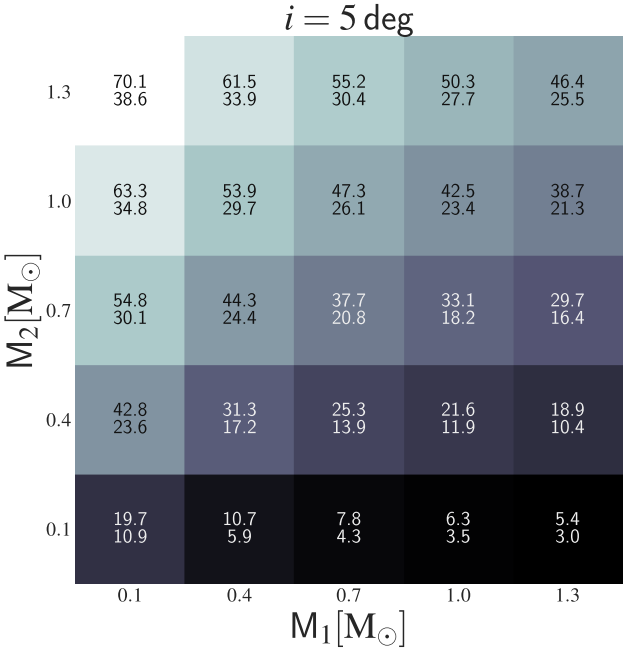

Figure 8. RV semi-amplitude (K_2) values for a series of M_1 and M_2 configurations according to the binary mass function. The values are in km s^{-1} and are given for $P_{\rm orb} = 0.5$ and 3 h for top and bottom values in each cell, for representative binary orbits.

but even this source remains unconvincing based on available data. For $P_{\rm orb} \simeq$ hours WD-hosting binaries with $i = 5$ deg, one would still expect a semi-amplitude of > 10 km s^{-1} (Fig. 8), excepting extremely low-mass WD companions (which, although capable of housing significant magnetic field strengths as per Hardy, Dufour & Jordan 2023, would require relatively rare products of binary evolution). Longer baseline and additional measurements are be needed to properly rule on the presence of RV variability in sources we have shown here, with the expected signatures being in the grasp of such observations. Only one source analysed as part of our RV investigations was detected in our searches for photometric variability in the vicinity of GLEAM-X J1627−52, source ID 548, whose ULTRACAM and VVV light curves are shown in Appendix C. ULTRACAM data were found to harbour no obvious periodic features following our analysis in Section 3.1. The source is at the limit of VVV data (typically a 5σ detection per epoch) with a $K_s = 18.4$ mag. The light curve displays no variability beyond statistical noise, in line with our results from all VVV sources in Section 4.1. A final note is to state that on spatial density alone, one would not expect such a number of short-period binary systems in a search of 0.125 arcmin^2, further casting doubt on their origin. Overall, we do not consider our measured RV curves to show any strong evidence of a counterpart system.

When considering a non-binary source system, Rea et al. (2024) suggest that isolated magnetic WDs emitting beamed dipole radiation are a more attractive proposition to explain sources such as GLEAM-X J1627−52 than NSs, at least in terms of expected numbers and so constraints on their presence are of interest (in the binary scenario, they will be outshone by their companion). As those authors additionally note however, the known population of isolated, magnetic WDs fall significantly short of the requirements for radio emission in the pulsar scenario (typically by a factor $\gtrsim$100 in magnetic field strength), and so some form of binary interaction remains favoured

Downloaded from https://academic.oup.com/mnras/article/538/2/925/8029896 by guest on 26 March 2025

for their interpretation. For identifying nearby isolated WDs, our observations largely do not reach the required sensitivity.

An isolated (or otherwise wide-binary) magnetar interpretation remains viable with our lack of a counterpart detection. Indeed, spectra of such objects may appear as red, largely featureless, spectra (Hare et al. 2024), which are abundant in the vicinity of GLEAM-X J1627−52 (Fig. B1). Although the optical and NIR emission of magnetars is relatively poorly understood, largely due to the difficulty in observations (Mignani et al. 2009; Chrimes et al. 2022), they are known to be subtly variable on short time-scales linked to their spin period (Dhillon et al. 2011), as well as more dramatically on longer time-scales of years (Lyman et al. 2022). The origin of this longer time-scale emission is unclear, but, nevertheless, monitoring of this location with deep NIR observations over a significant baseline could reveal any such long-time-scale variability to identify a putative magnetar counterpart.

A multiwavelength counterpart of GLEAM-X J1627−52 remains elusive, despite extensive efforts to find it, including this work. The comparatively poor localization and crowded field make it impossible to identify a single candidate based only on spatial coincidence. With the recent results of Hurley-Walker et al. (2024) and Ruiter et al. (2024), our understanding of the optical counterpart population of long-period radio transients is growing. A deeper understanding of the detectability and characteristics of this population will allow us to revisit GLEAM-X J1627−52 with renewed prior information to better quantify our ability to extract the counterpart from the data.

6 CONCLUSION

We have presented a comprehensive search for optical and NIR variability in the vicinity of the long-period radio transient GLEAM-X J1627−52 and found no convincing counterpart. We obtain the following conclusions.

(i) The local stellar population, characterized by MUSE optical spectra, is dominated by low-mass K/M stars with no strong spectral peculiarities identified, although our sensitivity is not sufficient to probe the typical luminosities of isolated WDs.

(ii) No source was found to exhibit periodicity or variability in either high-speed optical ULTRACAM data taken at 10 s cadence over a period of 1.9 h, or lower-cadence NIR VVV survey epochs with revisit times of weeks over a period of ~ 3 yr.

(iii) Two Balmer emission line sources were identified, but their characteristics are adequately described by chromospheric activity in isolated M-dwarfs and are unlikely to indicate a close WD binary counterpart.

(iv) No source exhibits an RV curve strongly showing expectations for a close binary system with $P_{\rm orb} \lesssim$ hours, ruling out their presence to our limits (excluding the possibility of an almost-face-on system). What RV variation is seen for a few sources is likely due to other astrophysical considerations (e.g. rotation, Jenkins et al. 2009) or under estimated uncertainties.

(v) We rule out the presence of a hot subdwarf in the localization, which we would have expected to detect at high SNR.

(vi) We determine our search is insensitive to an (effectively) isolated magnetar or WD, or compact binary system (WD/NS + WD/NS) counterpart, and so they remain viable scenarios.

(vii) Most close binary systems RV amplitudes are within reach of MUSE even for highly inclined systems, but further monitoring is needed to provide robust evidence of any close-binary system(s) with interesting periods.

(viii) Further observations of GLEAM-X J1627−52 during an active radio phase with high spatial resolution, which will allow for an unambiguous spatial association with a presented MUSE (or a hitherto undetected) source found during a radio-quiet period, may be the most likely route to unambiguously identifying its counterpart.

ACKNOWLEDGEMENTS

We thank the anonymous reviewer for suggestions that improved the clarity of the manuscript. JDL acknowledges support from a UK Research and Innovation (UKRI) Future Leaders Fellowship (MR/T020784/1). VSD and ULTRACAM are funded by the Science and Technology Facilities Council (STFC, grant ST/Z000033/1). SKA acknowledges funding from UKRI in the form of a Future Leaders Fellowship (grant nos MR/T022868/1 and MR/Y034147/1). AAC acknowledges support through the European Space Agency (ESA) research fellowship programme. AJL has received funding from the European Research Council (ERC) under the European Union's Seventh Framework Programme (FP7-2007-2013) (grant agreement no. 725246). IP acknowledges support from a Royal Society University Research Fellowship (URF\R1\231496). DTHS acknowledges support from the STFC (grant nos ST/T007184/1, ST/T003103/1, ST/T000406/1, and ST/Z000165/1).

This publication makes use of data products from the Two Micron All Sky Survey, which is a joint project of the University of Massachusetts and the Infrared Processing and Analysis Center/California Institute of Technology, funded by the National Aeronautics and Space Administration and the National Science Foundation.

This work made use of ASTROPY:[6] a community-developed core PYTHON package and an ecosystem of tools and resources for astronomy (Astropy Collaboration 2013, 2018, 2022).

Based on observations collected at the European Organisation for Astronomical Research in the Southern Hemisphere under ESO programme(s) 108.23MN.

DATA AVAILABILITY

Raw and processed data used are available via the ESO data archives. Data used in the analysis or presented in figures are available upon reasonable request to the corresponding author.

REFERENCES

Astropy Collaboration, 2013, A&A, 558, A33
Astropy Collaboration, 2018, AJ, 156, 123
Astropy Collaboration, 2022, ApJ, 935, 167
Bacon R. et al., 2010, Proc. SPIE, Vol. 7735, The MUSE Second-generation VLT Instrument. SPIE, California, US, p. 773508
Barbary K., 2018, Astrophysics Source Code Library, record ascl:1811.004
Beniamini P., Wadiasingh Z., Hare J., Rajwade K. M., Younes G., van der Horst A. J., 2023, MNRAS, 520, 1872
Bertin E., Arnouts S., 1996, A&AS, 117, 393
Bradley L. et al., 2024, astropy/photutils: 1.13.0. Zenodo. Available at: https://doi.org/10.5281/zenodo.12585239
Buchner J., 2016, Stat. Comput., 26, 383
Buchner J., 2019, PASP, 131, 108005
Buchner J., 2021, J. Open Source Softw., 6, 3001
Caleb M. et al., 2022, Nat. Astron., 6, 828
Chatterjee P., Hernquist L., Narayan R., 2000, ApJ, 534, 373

[6] http://www.astropy.org

Downloaded from https://academic.oup.com/mnras/article/538/2/925/8029896 by guest on 26 March 2025

Chen K., Ruderman M., 1993, ApJ, 402, 264
Chime/Frb Collaboration, 2023, ApJ, 947, 83
Chrimes A. A., Levan A. J., Fruchter A. S., Groot P. J., Kouveliotou C., Lyman J. D., Tanvir N. R., Wiersema K., 2022, MNRAS, 512, 6093
Cordes J. M., Chatterjee S., 2019, ARA&A, 57, 417
Cross N. J. G. et al., 2012, A&A, 548, A119
Culpan R., Geier S., Reindl N., Pelisoli I., Gentile Fusillo N., Vorontseva A., 2022, A&A, 662, A40
Dhillon V. S. et al., 2007, MNRAS, 378, 825
Dhillon V. S. et al., 2011, MNRAS, 416, L16
Dhillon V. S. et al., 2021, MNRAS, 507, 350
de Ruiter I. et al., 2024, preprint (arXiv:2408.11536)
Dong F. A. et al., 2024, preprint (arXiv:2407.07480)
Duncan R. C., Thompson C., 1992, ApJ, 392, L9
Flaugher B. et al., 2015, AJ, 150, 150
Fossati M. et al., 2019, MNRAS, 490, 1451
Freudling W., Romaniello M., Bramich D. M., Ballester P., Forchi V., García-Dabló C. E., Moehler S., Neeser M. J., 2013, A&A, 559, A96
Gaia Collaboration, 2023, A&A, 674, A1
Garnavich P., Littlefield C., Kafka S., Kennedy M., Callanan P., Balsara D. S., Lyutikov M., 2019, ApJ, 872, 67
Gentile Fusillo N. P. et al., 2021, MNRAS, 508, 3877
Ginsburg A. et al., 2019, AJ, 157, 98
Hardy F., Dufour P., Jordan S., 2023, MNRAS, 520, 6111
Hare J., Pavlov G. G., Posselt B., Kargaltsev O., Temim T., Chen S., 2024, ApJ, 972, 176
Hurley-Walker N. et al., 2022, Nature, 601, 526
Hurley-Walker N. et al., 2023, Nature, 619, 487
Hurley-Walker N. et al., 2024, ApJL, 976, L21
Husser T. O., Wende-von Berg S., Dreizler S., Homeier D., Reiners A., Barman T., Hauschildt P. H., 2013, A&A, 553, A6
Husser T.-O. et al., 2016, A&A, 588, A148
Hyman S. D., Lazio T. J. W., Kassim N. E., Ray P. S., Markwardt C. B., Yusef-Zadeh F., 2005, Nature, 434, 50
Ibañez Bustos R. V., Buccino A. P., Flores M., Martinez C. F., Mauas P. J. D., 2023, A&A, 672, A37
Ivanov V. D., Coccato L., Neeser M. J., Selman F., Pizzella A., Dalla Bontà E., Corsini E. M., Morelli L., 2019, A&A, 629, A100
Jenkins J. S., Ramsey L. W., Jones H. R. A., Pavlenko Y., Gallardo J., Barnes J. R., Pinfield D. J., 2009, ApJ, 704, 975
Kamann S., 2018, Astrophysics Source Code Library, record ascl:1805.021
Kamann S., Wisotzki L., Roth M. M., 2013, A&A, 549, A71
Kamann S. et al., 2016, A&A, 588, A149
Katz J. I., 2017, ApJ, 835, 150
Katz J. I., 2022, Ap&SS, 367, 108
Kesseli A. Y., West A. A., Veyette M., Harrison B., Feldman D., Bochanski J. J., 2017, ApJS, 230, 16
Konar S., 2023, JA&A, 44, 1
Kumar V., Rajpurohit A. S., Srivastava M. K., Fernández-Trincado J. G., Queiroz A. B. A., 2023, MNRAS, 524, 6085
Lanman A. E. et al., 2022, ApJ, 927, 59
Lee Y. W. J. et al., 2025, preprint (arXiv:2501.09133)
Li D. et al., 2024, preprint (arXiv:2411.15739)
Loeb A., Maoz D., 2022, Res. Notes Am. Astron. Soc., 6, 27
Lofthouse E. K. et al., 2020, MNRAS, 491, 2057
Lyman J. D., 2021, Astrophysics Source Code Library, record ascl:2103.003
Lyman J. D., Levan A. J., Wiersema K., Kouveliotou C., Chrimes A. A., Fruchter A. S., 2022, ApJ, 926, 121
Lyne A. G., Manchester R. N., Taylor J. H., 1985, MNRAS, 213, 613
Manchester R. N., Hobbs G. B., Teoh A., Hobbs M., 2005, AJ, 129, 1993
Marsh T. R., Duck S. R., 1996, MNRAS, 278, 565
Marsh T. R. et al., 2016, Nature, 537, 374
McLaughlin M. A. et al., 2006, Nature, 439, 817
Mignani R. P. et al., 2009, A&A, 497, 451
Minniti D. et al., 2010, New Astron., 15, 433
Naylor T., 1998, MNRAS, 296, 339
Newton E. R., Irwin J., Charbonneau D., Berlind P., Calkins M. L., Mink J., 2017, ApJ, 834, 85
Olausen S. A., Kaspi V. M., 2014, ApJS, 212, 6
Pacini F., 1967, Nature, 216, 567
Pelisoli I. et al., 2023, Nat. Astron., 7, 931
Pelisoli I. et al., 2024, MNRAS, 527, 3826
Pickles A. J., 1998, PASP, 110, 863
Press W. H., Rybicki G. B., 1989, ApJ, 338, 277
Rea N., Borghese A., Esposito P., Coti Zelati F., Bachetti M., Israel G. L., De Luca A., 2016, ApJ, 828, L13
Rea N. et al., 2022, ApJ, 940, 72
Rea N. et al., 2024, ApJ, 961, 214
Reiners A., Joshi N., Goldman B., 2012, AJ, 143, 93
Rodriguez A. C., 2025, preprint (arXiv:2501.03315)
Roulston B. R., Green P. J., Kesseli A. Y., 2020, ApJS, 249, 34
Skrutskie M. F. et al., 2006, AJ, 131, 1163
Soto K. T., Lilly S. J., Bacon R., Richard J., Conseil S., 2016, MNRAS, 458, 3210
Stellingwerf R. F., 1978, ApJ, 224, 953
Stetson P. B., 1987, PASP, 99, 191
Suvorov A. G., Melatos A., 2023, MNRAS, 520, 1590
Thompson C., Duncan R. C., 1995, MNRAS, 275, 255
Tong H., 2023, ApJ, 943, 3
Weilbacher P. M. et al., 2020, A&A, 641, A28

APPENDIX A: OPTICAL SOURCES IN THE VICINITY OF GLEAM-X J1627

In Table A1, we show the coordinates for those sources specifically addressed in the text or figures of this work, as well as all those detected within 4 arcsec (2σ localization) of GLEAM-X J1627−52. The sources were also photometered using a white-light image of the MUSE data cube. This was calibrated to *Gaia G* band using cross matches within the FoV. MUSE does not extend as blue as *Gaia G* band (cutting off at 470 and 400 nm, respectively), although typically differences between the two magnitudes are $\lesssim 0.1$ mag. *Gaia* cross-matches were found through a cone search of Data Release 3. The sources were photometered using SEP (Barbary 2018); magnitudes are not presented for insignificant detections.

Downloaded from https://academic.oup.com/mnras/article/538/2/925/8029896 by guest on 26 March 2025

Table A1. Data for sources in the vicinity of GLEAM-X J1627−52 analysed during this work. All sources within 2σ of the localization or otherwise mentioned in the manuscript are included. $M_{\rm MUSE}$ is the magnitude of the source in a white-light image of the MUSE data cube, calibrated to *Gaia G* band. 'Separation' is that of the source from GLEAM-X J1627−52. 'ULTRACAM' and 'VVV' denote if the source was also detected and analysed in those data (see the text).

ID	*Gaia* DR3 ID	RA (deg)	Dec. (deg)	$M_{\rm MUSE}$ (AB mag)	$\sigma(M_{\rm MUSE})$ (AB mag)	Separation (arcsec)	ULTRACAM	VVV	RV	Emission
247	5933733753139994240	246.99647	−52.58764	20.81	0.04	11.64			✓	
254	—	247.00011	−52.58751	—	—	11.75			✓	
267	—	247.00052	−52.58725	21.92	0.06	11.33			✓	
268	—	246.99664	−52.58717	—	—	9.92			✓	
273	—	246.99539	−52.58707	23.01	0.11	10.69			✓	
278	—	247.00093	−52.58684	—	—	10.62			✓	
279	—	246.99452	−52.58686	23.19	0.12	11.19			✓	
282	—	247.00017	−52.58679	—	—	9.51			✓	
285	5933733753138856832	246.99906	−52.58672	20.39	0.03	8.29	✓	✓	✓	
287	5933733753139670912	246.99639	−52.58665	20.96	0.04	8.35	✓		✓	
291	5933733753136325504	247.00168	−52.58666	19.92	0.03	11.27	✓	✓	✓	
295	—	246.99942	−52.58657	21.46	0.05	8.05			✓	
299	—	246.99591	−52.58651	23.17	0.12	8.37			✓	
300	—	246.99542	−52.58649	22.92	0.10	8.94			✓	
306	—	246.99820	−52.58627	21.11	0.04	6.30		✓	✓	
309	—	247.00129	−52.58624	22.71	0.09	9.62			✓	
313	5933733753136323968	247.00254	−52.58622	19.82	0.02	11.81			✓	
314	—	246.99694	−52.58612	—	—	6.10			✓	
318	—	246.99795	−52.58604	—	—	5.43			✓	
319	—	246.99636	−52.58603	21.69	0.06	6.39			✓	✓
320	—	246.99508	−52.58602	21.58	0.05	8.21	✓		✓	
324	—	247.00072	−52.58600	21.80	0.06	8.09			✓	
335	—	247.00155	−52.58572	22.85	0.10	9.02			✓	
336	—	247.00091	−52.58570	—	—	7.79	✓		✓	
339	—	247.00282	−52.58570	22.00	0.07	11.53			✓	✓
340	—	246.99598	−52.58567	22.24	0.07	5.90			✓	
344	—	247.00247	−52.58566	22.36	0.08	10.76			✓	
345	—	246.99747	−52.58563	—	—	4.10			✓	
348	—	247.00165	−52.58557	21.92	0.06	8.98			✓	
349	—	246.99828	−52.58551	23.06	0.11	3.62			✓	
350	—	247.00215	−52.58557	22.37	0.08	9.98			✓	
351	—	246.99328	−52.58553	—	—	10.76			✓	
354	—	246.99667	−52.58546	23.23	0.12	4.34			✓	
359	—	246.99865	−52.58542	22.70	0.09	3.60			✓	
360	5933733753136360448	246.99401	−52.58539	19.69	0.02	9.09	✓	✓	✓	
367	5933733753138853248	246.99826	−52.58525	20.59	0.03	2.72	✓	✓	✓	
370	—	246.99464	−52.58518	22.22	0.07	7.55			✓	
384	5933733753169960448	247.00197	−52.58494	19.01	0.02	9.00	✓	✓	✓	
385	—	247.00121	−52.58493	23.13	0.11	7.34			✓	
389	—	247.00063	−52.58484	23.34	0.13	6.03			✓	
390	—	246.99819	−52.58484	—	—	1.28			✓	
395	—	246.99357	−52.58481	—	—	9.57			✓	
396	—	246.99266	−52.58478	—	—	11.53			✓	
400	5933733753138309120	246.99949	−52.58470	20.15	0.03	3.49	✓	✓	✓	
412	—	247.00241	−52.58454	23.03	0.11	9.82			✓	
415	—	246.99704	−52.58447	—	—	1.93				
424	5933733753136357760	246.99768	−52.58430	20.16	0.03	0.96	✓	✓	✓	
435	5933733748823423104	246.99627	−52.58406	18.79	0.01	3.97	✓	✓	✓	
439	5933733753136354432	246.99958	−52.58400	19.43	0.02	4.10	✓	✓	✓	
443	—	246.99267	−52.58395	20.28	0.03	11.66			✓	
451	—	247.00310	−52.58382	23.23	0.12	11.61			✓	
454	—	246.99688	−52.58374	23.47	0.14	3.63				
455	—	246.99327	−52.58376	—	—	10.53			✓	
463	—	246.99507	−52.58362	22.04	0.07	7.04			✓	
467	—	246.99930	−52.58356	21.84	0.06	4.63			✓	
468	—	246.99756	−52.58356	—	—	3.58			✓	
469	—	246.99283	−52.58359	—	—	11.63			✓	
480	—	247.00284	−52.58340	23.12	0.11	11.50			✓	
494	—	247.00122	−52.58325	—	—	8.58			✓	
495	—	246.99940	−52.58328	—	—	5.55			✓	
496	—	246.99346	−52.58323	—	—	10.80			✓	

Downloaded from https://academic.oup.com/mnras/article/538/2/925/8029896 by guest on 26 March 2025

Table A1 – *continued*

ID	*Gaia* DR3 ID	RA (deg)	Dec. (deg)	$M_{\rm MUSE}$ (AB mag)	$\sigma(M_{\rm MUSE})$ (AB mag)	Separation (arcsec)	ULTRACAM	VVV	RV	Emission
525	5933733753138848640	246.99752	−52.58280	20.87	0.04	6.29			✓	
526	—	246.99875	−52.58277	22.17	0.07	6.60			✓	
529	5933733753138311168	246.99550	−52.58267	20.44	0.03	8.52	✓	✓	✓	
534	—	246.99600	−52.58256	22.64	0.09	8.23			✓	
539	—	247.00200	−52.58253	—	—	11.47			✓	
540	—	246.99960	−52.58252	—	—	8.10			✓	
547	—	247.00046	−52.58241	—	—	9.45			✓	
548	5933733753138848512	246.99783	−52.58242	20.54	0.03	7.61	✓	✓	✓	
557	—	246.99569	−52.58222	23.26	0.12	9.61			✓	
563	—	247.00115	−52.58209	20.91	0.04	11.26			✓	
564	—	246.99449	−52.58208	23.38	0.13	11.59			✓	
572	5933733753176404864	246.99810	−52.58195	20.09	0.03	9.31		✓	✓	
574	—	246.99979	−52.58195	21.24	0.05	10.16			✓	
575	—	246.99498	−52.58192	—	—	11.37			✓	
590	5933733753136366976	247.00056	−52.58171	18.04	0.01	11.68			✓	
591	—	246.99749	−52.58172	21.38	0.05	10.17		✓	✓	
592	—	246.99631	−52.58171	—	—	10.75			✓	
598	—	246.99941	−52.58157	22.90	0.10	11.14			✓	
599	—	246.99710	−52.58157	21.78	0.06	10.79			✓	

APPENDIX B: SPECTRA AND RADIAL VELOCITY CURVES OF NEARBY SOURCES

In Fig. B1, we show extracted spectra for all detected sources within 4 arcsec (2σ localization) of GLEAM-X J1627−52. In Fig. B2, we show RV curves of the subset of those sources where we were able to perform the analysis of Section 3.3 and determine an RV curve. Not shown are source IDs 454 and 415, for which we could not determine reliable RVs for enough individual epochs, and source IDs 359 and 468, which are presented in Figs 5 and 6, respectively.

Downloaded from https://academic.oup.com/mnras/article/538/2/925/8029896 by guest on 26 March 2025

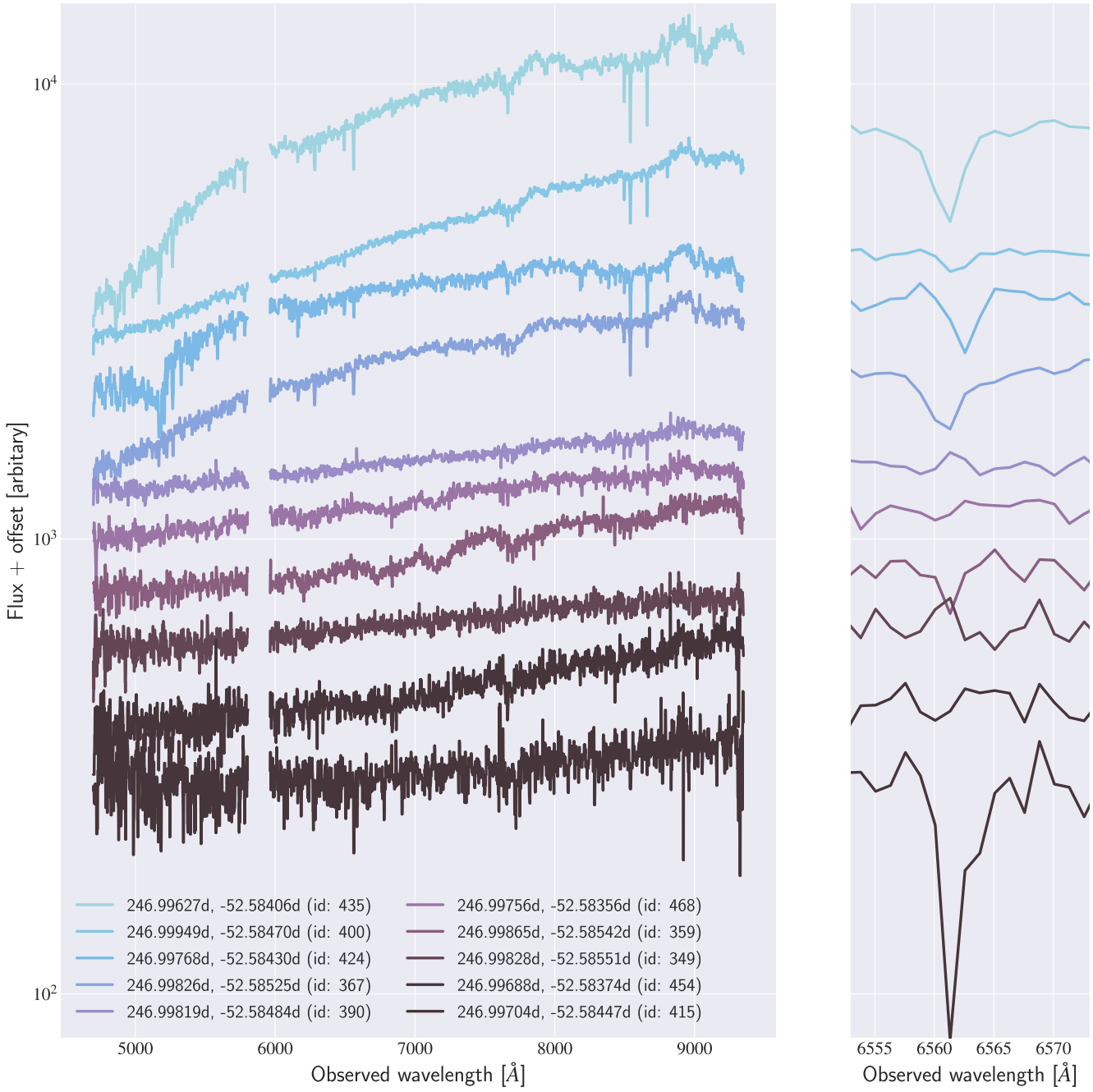

Figure B1. Extracted spectra of sources within the 2σ localization of GLEAM-X J1627−52. The right panel offers a zoom-in around the location of Hα. The legend indicates their right ascension and declination coordinates, with an accompanying source ID matching those of Table A1.

Downloaded from https://academic.oup.com/mnras/article/538/2/925/8029896 by guest on 26 March 2025

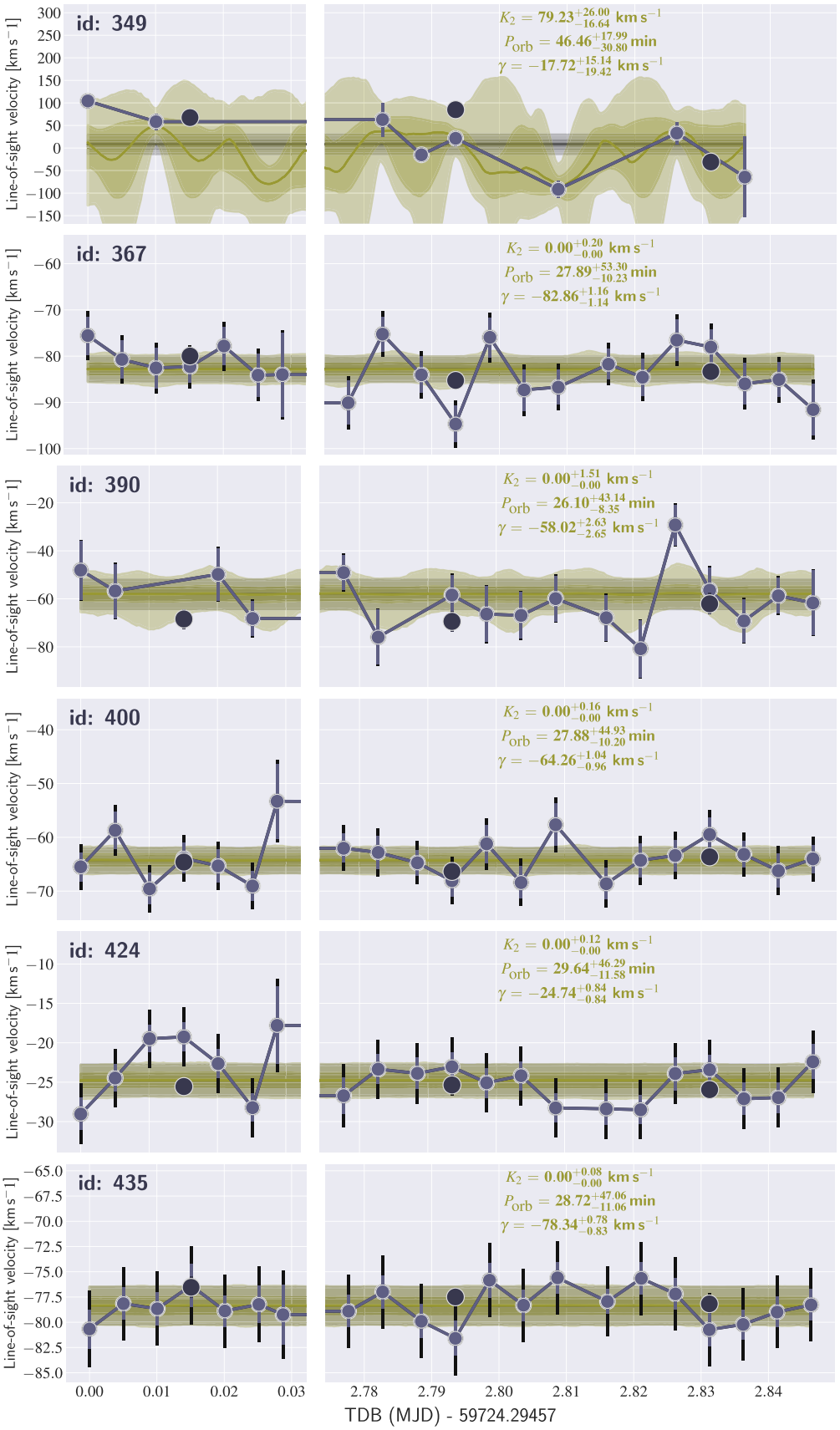

Figure B2. Same as Fig. 5, but shown for additional sources within the 2σ localization of GLEAM-X J1627−52.

Downloaded from https://academic.oup.com/mnras/article/538/2/925/8029896 by guest on 26 March 2025

APPENDIX C: LIGHT CURVE OF SOURCE ID 548

Source ID 548 is the only source which passed our initial quality checks for RV variability and was bright enough to be detected in our photometric searches of ULTRACAM and VVV data. Its light curve is shown in Figs C1 and C2. The source is significantly blended in ULTRACAM with source IDs 525 and 572, and a conjoined aperture encompassing these three was used. The data display no indications of periodic or outbursting variability, in line with all other sources searched photometrically (see Section 4.1 and Fig. 2).

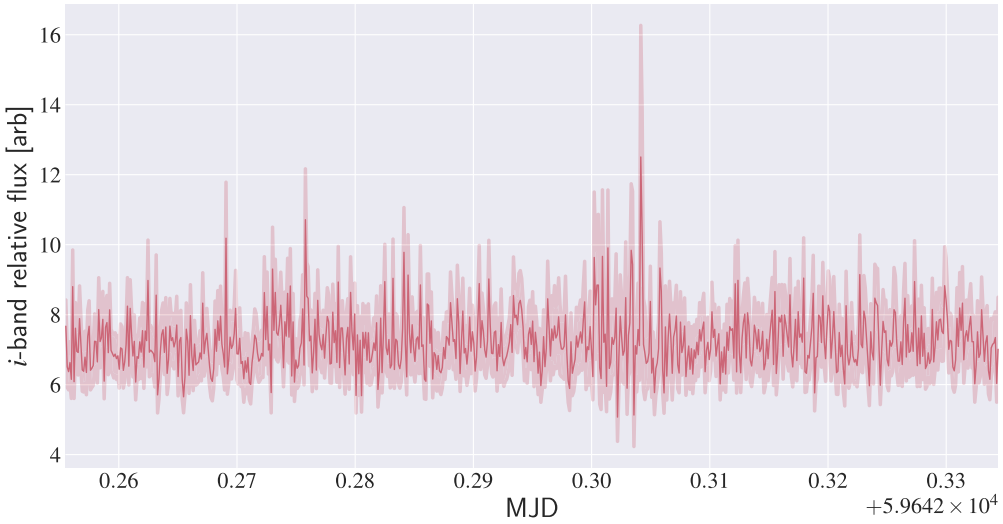

Figure C1. Light curve of aperture containing source ID 548 from ULTRACAM. The increase in noise at MJD = 59642.30−59642.35 is due to a deterioration of the atmospheric seeing. No periodic variability was found from analysis of this light curve (see the text).

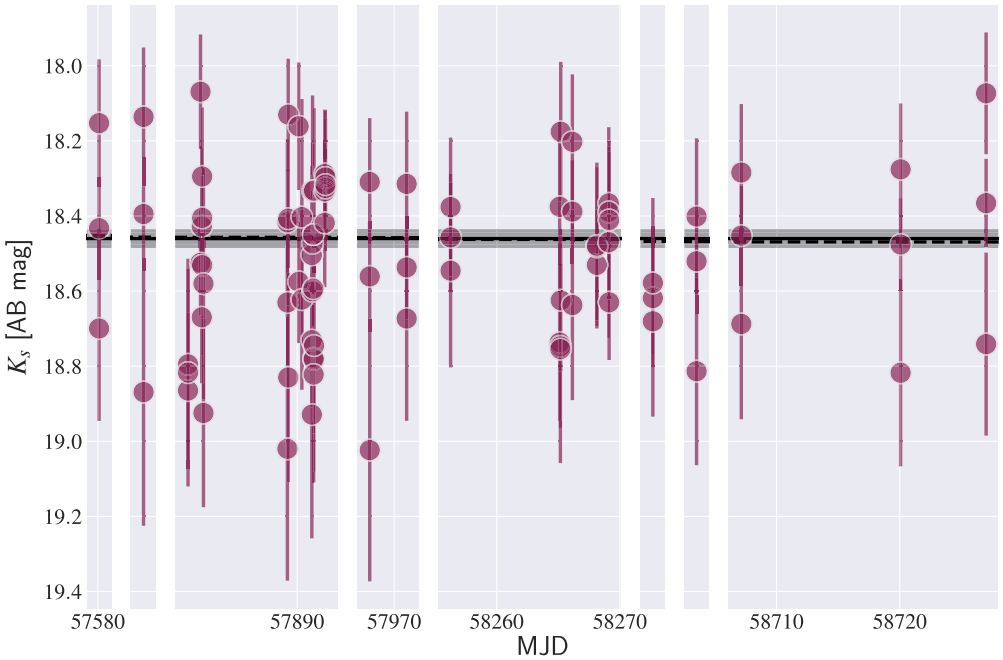

Figure C2. Light curve of source ID 548 from VVV. The solid black line and grey shaded region show the model fit of a light curve as a constant flux model. The (almost indistinguishable) dashed black line indicates the best linear in time fit to the flux evolution. There is no evidence of outbursting or variability in individual photometric measurements, nor a long-term evolution of the flux level of the source.

This paper has been typeset from a TEX/LATEX file prepared by the author.

© 2025 The Author(s).
Published by Oxford University Press on behalf of Royal Astronomical Society. This is an Open Access article distributed under the terms of the Creative Commons Attribution License (https://creativecommons.org/licenses/by/4.0/), which permits unrestricted reuse, distribution, and reproduction in any medium, provided the original work is properly cited.

Downloaded from https://academic.oup.com/mnras/article/538/2/925/8029896 by guest on 26 March 2025